Benefits of Mann–Kendall trend analysis for vibration-based condition monitoring

Adrien Marsick, Hugo André, Ilyes Khelf, Quentin Leclère, Jérôme Antoni

Mechanical Systems and Signal Processing 216 (2024) 111486

Contents lists available at ScienceDirect

Mechanical Systems and Signal Processing

journal homepage: www.elsevier.com/locate/ymssp

Benefits of Mann–Kendall trend analysis for vibration-based condition monitoring

Adrien Marsick [a,c,*], Hugo André [b], Ilyes Khelf [c], Quentin Leclère [a], Jérôme Antoni [a]

[a] INSA Lyon, LVA, UR, 69621 Villeurbanne, France
[b] Universite Jean Monnet Saint-Etienne, IUT de Roanne, LASPI, UR, F-42300, Roanne, France
[c] Engie Green, 6 Rue Alexander Fleming, 69007 Lyon, France

ARTICLE INFO

Communicated by Y. Lei

Keywords:
Trend analysis
Rank statistics
Mann–Kendall
Mannagram
Kendrum
Kurtogram
Cyclic spectral analysis
Condition monitoring
Wind turbine

ABSTRACT

Rank-based statistics offer an appealing framework to non-parametric robust trend detection. Especially, the Mann–Kendall test detects the presence of a trend in a series. This paper investigates the benefits of using the Mann–Kendall test, which seems to have remained largely unnoticed in the context of vibration-based condition monitoring. Two contributions structure the present paper. First, theoretical foundations of rank-statistics are reminded and the Z-score is introduced, a statistical metric measuring the presence of a trend in a given series. The performance of the Mann–Kendall test is investigated and confronted to different numerical cases involving series of increasing condition indicators. Second, based on this understanding, the Z-score metric is exploited to design two trend-oriented signal processing tools dedicated to vibration-based condition monitoring. Namely, a new tool named the *Mannagram* is introduced as a dyadic filterbank representation of the trend of indicators series. It shows effective in the informative band selection problem and unveils more interpretable indicators. Besides, a concise representation of trend by frequency bin is introduced and coined the *Kendrum*. This representation is shown to help the diagnosis by summarising the trend information of series of spectra. Both methods are demonstrated on run-to-failure series of vibration signals from industrial wind turbines.

1. Introduction

Modern condition monitoring relies on a wealth of indicators. The health condition of rotating machinery component is monitored by indicators stemming from physical measurements of the machine such as temperature [1], lubricant analysis [2], acoustic emission [3], instantaneous angular speed [4], electric signature [5] or vibration analysis [6]. The latter is widely preferred due to the richness of its information content and the extensive industrial and academic experience feedback. Scholars have dedicated their work to the design of tools aiming at fault detection, localisation, and prognosis from vibration signals. At the crossroads of tribology, mechanical modelling, and signal processing fields, the developed methods offer tools for the surveillance of gears and bearings using the fault signature properties. These tools can rely on the change of signal statistical distribution with an increase of vibration introduced by fault signature [7], change of sparsity properties [8,9], or on the detection of non-stationary waveforms by the means of an angular cyclicity [10–12] fed by numerous instantaneous rotation speed estimation methods [13]. Indeed, most of the faults on gears and bearings generate forces synchronous with a rotation of reference, yielding vibration signature with cyclic statistical properties [14]. The vibration signals received by the sensors may contain a cyclic fault signature distorted by a transmission path

* Corresponding author at: INSA Lyon, LVA, UR, 69621 Villeurbanne, France.
E-mail address: adrien.marsick@insa-lyon.fr (A. Marsick).

https://doi.org/10.1016/j.ymssp.2024.111486
Received 10 October 2023; Received in revised form 9 April 2024; Accepted 30 April 2024
Available online 10 May 2024

and covered by other sources with a low signal-to-noise ratio. The angular cyclicity of the fault signature with respect to a cycle of reference is often fixed by the geometry of the component (number of teeth/rolling elements, races diameters) opening the door to precise spectral analysis. The angle–time duality of the fault signature led to works on envelope analysis [15], spectral correlation [16], and has been partly solved by the class of angle–time cyclostationary signals [17]. The theoretical developments led to rich 1D or 2D spectral representations, where the frequency channels containing the diagnostic information are often narrowed down with prior knowledge about the geometry of the components and the kinematics of the machine. The angle–time duality of the fault signature often leads to a pre-processing step: the signal is observed in a informative frequency band with favourable SNR usually found around the structural resonances.

Based on a detailed analysis of the signals, a wealth of scalar indicators are built and monitored automatically. The processing of the multiple condition indicator series is itself a vast field with applications in fault detection and prognosis. As most of the indicators are designed to maximise the detection probability given false alarm constraints [10], they are expected to show an increase with incipient faults. Fault detection is made by comparing an indicator observation to a preset threshold to classify it. However, selecting an appropriate threshold is a complex task, and trend monitoring has largely been used as a complement to amplitude-based techniques. Trend monitoring is a vast research field in which the objective is often to extract simplified information from a given time series [18]. Rank-based statistics offer an appealing framework for such a task. They focus on the tidiness of a series with no prior on the distribution of the data with robustness to outliers and censoring. The Mann–Kendall test [19–21] evaluates the hypothesis H_0 that the series is independent and identically distributed against the hypothesis of a trend. From this framework, rank-based statistics have been used extensively to test for the presence of trends, especially in climatology time series [22–26] for their robustness. These appealing properties have attracted attention for condition monitoring applications for prognosis with a primary use for feature selection. Among the three common feature selection metrics for remaining useful life estimation, *prognosability, trendability and monotonicity*, rank-based trend tests have been used to evaluate the latter one [27–30]. Pinciroli et al. used the Mann–Kendall test for the fusion of a set of condition indicators formulated as a multi-objective optimisation problem [31]. With the same objective of monotonicity evaluation, Lyu et al. proposed a method to optimise the selection of sensors and indicators using the Mann–Kendall test and Sen's slope estimator for the monitoring of a helicopter transmission [32]. Regarding its use in fault detection, Guo and Rasmussen monitored an air conditioning system using a modified Mann–Kendall test [33].

Despite the use of trend analysis for prognosis in indicator fusion and monitoring, little has been done for diagnosis concerning dedicated trend-oriented signal processing tools. Partly due to the lack of available run-to-failure data-sets in the scientific community, most of the diagnostic techniques are tailored for a single vibration signal. Concerning the informative frequency band problem, the selection is based on a maximal value of the spectral feature (e.g. kurtosis, entropy, or cyclostationarity). However, such approach is hard to generalise since it is regularly jeopardised by other stronger sources in the signal accidentally showing the same spectral feature. The spectral analysis also suffers from the lack of proper trend monitoring techniques. Diagnostic information on a single spectrum may be complicated by the contrast between normally found peaks and the small increasing contribution of the fault signature.

The main idea of this paper is that a fault is better monitored by an increase rather than the absolute amplitude of a condition indicator. The innovation is to use rank-statistics trend indicators to build dedicated signal processing tools. The paper is organised in four main sections. Section 2 introduces the theoretical background on rank-based statistics. The Mann–Kendall test (MK test) is introduced in Section 2.1 and illustrated in 2.2. The different properties of these tests are investigated in Section 2.3. The main takeaway is the presentation of the *Z-score*, a transferable summarising scalar trend indicator. To demonstrate the capacities of the proposed tool, Section 3 presents the industrial dataset used in the following. From the insights given in the previous part, Section 4 presents a possible use of rank-based statistics for the informative frequency band selection problem. Using the same dyadic filter-bank representation as other *-grams* the introduced *mannagram* offers a concise representation of a fault-sensitive metric increase by frequency band. The concept is compared with the kurtogram and shows to point out favourable frequency bands. Section 5 applies the same concept for spectral analysis introducing the kendrum. The ability to focus on trends permits to better highlighting of the fault spectral signature.

2. Background on rank statistics

2.1. Trend test with Kendall rank-correlation

Rank correlation methods are a part of statistics that study the association between two variables having ordered categories. As defined by Kendall [21], one can study a set of n objects having two properties, $T = \{t_1, \dots, t_n\}$ and $Y = \{y_1, \dots, y_n\}$ they possess to a varying degree, defining two ranked series. An objective could be to test whether the two variables are correlated or not. Intuitively, if the two variables are positively correlated, one would expect the points (t_i, y_i) to be ordered on average. The expectation for a pair of points (i, j) would be that the agreement between the rankings of the two variables is preserved, that is $t_i < t_j$, $y_i < y_j$, or symmetrically, $t_i > t_j$, $y_i > y_j$. This latter defines a *concordant* pair, as opposed to a *discordant* pair for $t_i < t_j$, $y_i > y_j$. Negatively correlated data are expected to show discordant observations. On the other hand, when T and Y are independent, the set of concordant and discordant pairs are compensated. To study this intuitive vision of correlation, Kendall [19] proposed a new correlation measure based on the concordance of the ordered series (T, Y). The Kendall $\tau(n)$ coefficient for the series of the first n terms is defined as

$$\tau(n) = \frac{\text{number of concordant pairs} - \text{number of discordant pairs}}{\text{total number of pairs}}, \tag{1}$$

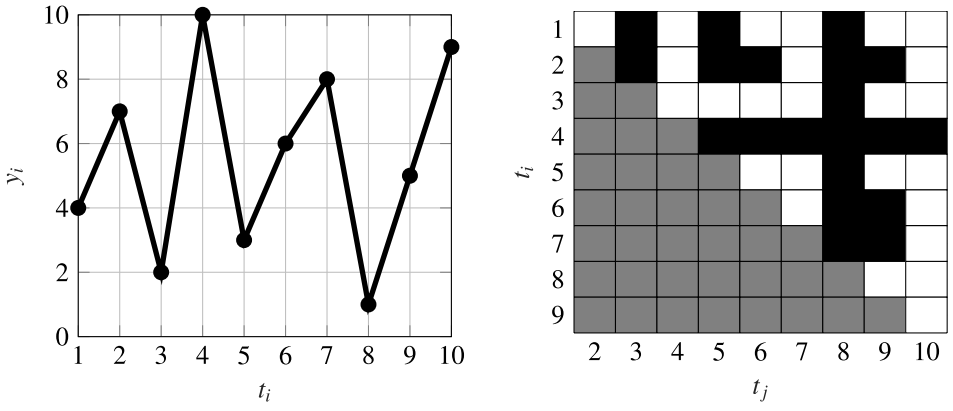

Fig. 1. Series (T, Y) of $n = 10$ points (a), and the matrix representation of each pair (b), allotting a score of +1 for concordant (white), −1 for discordant (black) and 0 values in grey. The series is taken from an example in [19].

or more explicitly

$$\tau(n) = 2\frac{S(n)}{n(n-1)}, \tag{2}$$

where the sum term S is expressed as

$$S(n) = \sum_{1\le i<j\le n} \operatorname{sgn}(t_i - t_j)\operatorname{sgn}(y_i - y_j), \tag{3}$$

where $\operatorname{sgn}(\cdot)$ is the sign function. The Kendall's τ is well defined as a correlation coefficient since its value ranges between −1 and +1. If the series is perfectly ordered, all the pairs are concordant yielding a value of $\tau = +1$, with the opposite case for anti-correlated data. If the two variables (T, Y) are independent, the Kendall's τ correlation coefficient should be close to zero. Further, in a context of monitoring, the time variable t_i with $i = \{1, \dots, n\}$ is usually already sorted chronologically. As such, the series will have the index of the signal as a X-axis, $t_i = i$ in what follows.

The sum variable $S(n)$ can be viewed as the sum of a rank matrix containing the comparison between each pair. For example, Fig. 1(a) presents a series (T, Y) of 10 points, where the matrix representation of the pair-to-pair comparison is shown in Fig. 1(b). The first line represents the comparison of the first point y_1 with respect to the remaining $y_2, \dots, y_{10}$. For each comparison, a score of +1 is allotted for a concordant pair and −1 in the opposite case. The sum variable $S(10)$ represent the sum of all the terms in the matrix. The Kendall's τ is found by dividing the result by the maximum number of pairs, that is the number of cells on the upper triangular matrix.

Intuitively, under the hypothesis H_0 that the points are sampled from the same continuous distribution function in the series (T, Y), the number of concordant and discordant pairs should even out [20]. In this case, Kendall derived the exact distribution of S and τ. Under the H_0 hypothesis, the expected value is null and the distribution of S is asymptotically Gaussian with a variance $\sigma^2_{S_0}$ of

$$\sigma^2_{S_0}(n) = \frac{n(n-1)(2n+5)}{18}. \tag{4}$$

It was shown that the distribution of S for independent and identically distributed series tends very quickly to a Gaussian distribution ($n = 10$ or greater) [19]. This key property has been used to design a non-parametric test to assess the presence of a monotonic trend in a time series. The rejection of the H_0 hypothesis implies that the different points in the series are not independent and identically distributed (iid). The practical interpretation is that an iid series shows no trend, and the non-acceptance of the test has been widely taken as evidence of the presence of a trend, defined as a constraint on the cumulative distribution functions [20]. No assumption on the distribution of the data is needed, and by construction, the test variable is less sensitive to outliers than least squares based methods.

For comparison purposes, the Z-score is introduced as a standardised version of the sum variable S, under the H_0 hypothesis

$$Z = \frac{S - \operatorname{sgn}(S)}{\sigma_{S_0}}, \tag{5}$$

that is the normalised distance to the H_0 [21] hypothesis. The $\operatorname{sgn}(S)$ adjustment comes from the consideration of the discontinuous distribution of S compared to the continuous Gaussian distribution. This is known as the*correction for continuity* [see21, chap. 4]. The rejection of H_0 is given by the condition $Z > Z_{\text{lim}}$ where the confidence is given by $p(Z > Z_{\text{lim}}) = \alpha$. This test is usually coined the Mann–Kendall test (MK test) [19,20]. Yue et Pilon [34] compared the performance of the MK test compared to slope-based

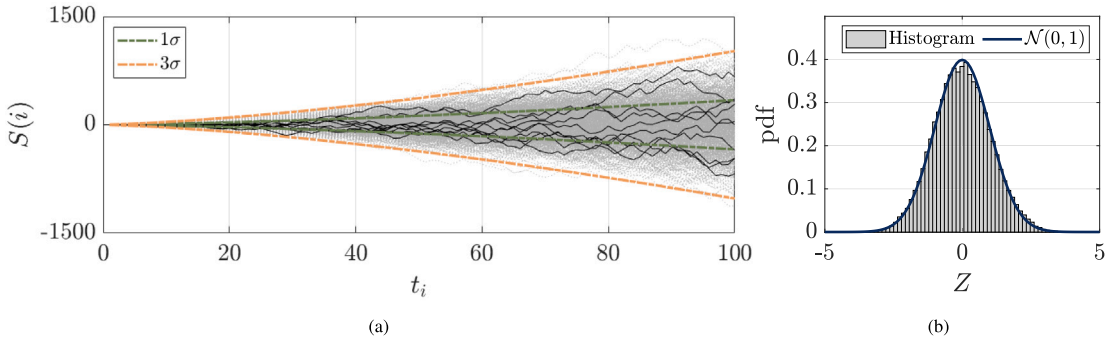

Fig. 2. Statistics for 1000 sampled series of 100 points with (a) the sum variable $S(i)$ along with the boundaries of unit standard deviation (green) and 3 standard deviations (yellow) and (b) the histogram of the normalised sum variable for $t_i > 10$, alongside with the probability density function of a normalised Gaussian distribution (blue).

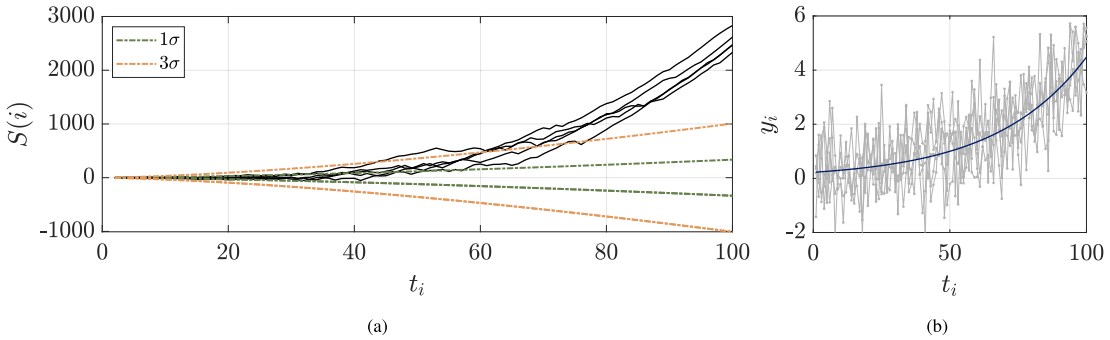

Fig. 3. Case of an exponential increase with (a) Sum variable for 5 exponential series $y_i = \exp\{1.5(i-50)/50\} + \epsilon_i$, where the noise ϵ_i is Gaussian with unit variance, along with the boundaries of standard deviation; (b) the corresponding series (grey solid lines) and the noiseless exponential (blue solid lines).

test. They showed that while the two frameworks do not really differ for normally-distributed data, the rank-based test greatly outperforms slope-based tests for non-Gaussian cases. By looking at the tidiness structure of the series, non regular sampling and missing data have little influence on the results of rank-based statistics. In this work, the Mann–Kendall trend test is used in its original formulation [19,20]. The original framework has been extended to overcome the initial limitations, with management of ties [35] in the series, to account for seasonality [36,37] and temporal correlation [22,34,38].

2.2. Example

To illustrate the previous concepts, synthetic numeric examples are shown in Fig. 2(a). Multiple series without trend are generated with a null mean and unit variance normally distributed data. A set of stationary series is generated where $t_i = i$ and $y_i \sim \mathcal{N}(0,1), n = 1,\dots,N$. For each series the sum variable $S(i)$ is calculated by chronologically adding the new points in the series. Fig. 2(a) presents a set of 1000 sum series $S(i)$ calculated from the sampled series y_i. The green and yellow lines correspond respectively to the boundaries of $\sigma_{S_0}(n) = \pm 1$ and $\sigma_{S_0}(n) = \pm 3$. As predicted, the sum variable S statistically stays within the boundaries defined by the standard deviation. Fig. 2(b) presents the histogram of the Z-score where the first 10 points are removed. Under the hypothesis H_0, the distribution is readily fitting to a normalised Gaussian.

If a trend is hidden in the series, more concordant pairs will be added in the rank matrix of Fig. 1(b). It will eventually make the sum variable deviate outside the confidence bounds of the H_0 assumption regardless on the initial distribution of the data around the trend. Since the Z-score is an image of the tidiness of the series, the index of first detection depends on the ratio of noise's variance against the slope of the trend.

This makes rank-statistics particularly efficient for cases of an exponential increase of a condition indicator. This is a difficult case for thresholding strategies based on a change in the mean. Fig. 3(a) presents 5 series of sum variable along with the boundaries of the H_0 standard deviation corresponding to the series of Fig. 3(b). The series were designed with an exponential increase of $y_i = \exp\{1.5(i-50)/50\} + \epsilon_i$ where the noise ϵ_i is Gaussian with unit variance. Even with the presence of noise, the average structure of the sum matrix of Fig. 1 is biased towards the addition of concordant pairs, with limited negative contributions. The sum variable deviates from the zero position and the change becomes statistically detectable whenever it crosses a preset boundary, tunable with a statistical $1-\alpha$ confidence. For a confidence of $Z_{\text{lim}} = 3$, the rejection of the H_0 hypothesis leads to a detection around index 70.

2.3. Expected distribution of detection indices for the occurrence of a deterministic trend

From a monitoring point of view, the hypothesis of a trend hidden in the series from the beginning of the observation window is improbable. Most of the time, one faces a section without trend corresponding to an initial state (undetected fault or stable defect) and followed by an increase of the health indicators. For a fixed confidence threshold, the detection index depends on the number of points taken into account and the initial distance to the $Z_{\lim}$ boundary before the change, normally distributed as previously seen. While not designed as a change-point test, an abrupt change will eventually accumulate sufficient concordant points to deviate from the H_0 hypothesis. One valuable piece of information is the number M of new incoming points in the series that are necessary to reject the H_0 hypothesis for a transition happening at index $t_i = l$ with $1-\alpha$ confidence. Since only the rank information is used in the proposed framework, the delay index M needed to detect the transition is a function of the total number of points taken into account in the series.

As a first didactic case, let a series be iid before a transition index l with the following M points perfectly ordered and greater than the precedent points. In this case, the added contribution of incoming points to the sum variable of Eq. (3) is known, with simple considerations on the structure of the rank matrix. In the case of perfectly ordered continuation where all the pairs are concordant, $t_i < t_j, y_i < y_j$, for $i \in [1, l+M]$ and $j \in [l+1, l+M]$, the sum variable $S(l+M)$ at index $l+M$ is

$$S(l+M) = S(l) + C(l,M), \tag{6}$$

where $C(l,M) = \sum_{m=0}^{M-1}(l+m)$ in this case and the prior sum term $S(l) \sim \mathcal{N}(0, \sigma^2_{S_0}(l))$ assumes the previous stationarity of the series. The Z-score at index $l+M$ reads

$$Z(l+M) = a(M)Z(l) + b(M), \tag{7}$$

where $a(M) = \frac{\sigma_{S_0}(l)}{\sigma_{S_0}(l+M)}$, $b(M) = \frac{C(l,M)}{\sigma_{S_0}(l+M)}$. The distribution of the rejection index $l+M$ is determined from the law of Eq. (7). With increasing M, the distribution of $Z(l+M)$ is shifted away from 0 by the increasing C, and a decreasing variance with $\frac{\sigma^2_{S_0}(l)}{\sigma^2_{S_0}(l+M)} < 1$. Given a predefined deviation threshold Z_{lim}, the probability of having a detection the index $l+M$ is

$$p\left(Z(l+M-1) \leq Z_{\lim} \quad Z(l+M) > Z_{\lim}\right), \tag{8}$$

which gives, using Eq. (7),

$$p\left(\frac{Z_{\lim} - b(M)}{a(M)} < Z(l) \leq \frac{Z_{\lim} - b(M-1)}{a(M-1)}\right), \tag{9}$$

which leads to

$$F\left(\frac{Z_{\lim} - b(M-1)}{a(M-1)}\right) - F\left(\frac{Z_{\lim} - b(M)}{a(M)}\right), \tag{10}$$

where F is the cumulative distribution function of the standardised Gaussian distribution $\mathcal{N}(0,1)$.

Additionally, as a simplified piece of information, the number of delay indices M for which the Z-score is expected to exceed a predefined deviation $Z_{\lim}$ threshold is given using Eq. (7), by the solution for M of,

$$\mathbb{E}\{Z(l+M)\} = Z_{\lim}, \tag{11}$$

where M can be found as the root of a polynomial described in Appendix.

Fig. 4(a) presents the different delay detection indices M expected for the MK test for different confidence intervals corresponding to $Z = 1, 2, 3$, as a function of the initial transition index l. The initial transition index l reflects the length of the studied series. The theoretical indices of Fig. 4(a) show reasonable reaction time to detect a trend in the series with limited variations with respect to the total length of the series. As derived in Appendix, it is shown that the delay index M grows as $O(l^{1/2})$, meaning that the relative detection delay with respect to the length of the series is expected to decrease with greater observation windows. Fig. 4(b) presents the theoretical distribution of the detection index M with the assumptions of a sharp transition at index $l = 80$. The black vertical dashed line represents the corresponding theoretical values calculated from Fig. 4(a) for expected indices. The distribution of detection indices is skewed. Knowing the expected detection delay for a change is valuable to design condition monitoring strategies.

This simple model permits a better understanding of the delay index distribution but is limited by two assumptions: the transition is sharp (all the points are higher than the previous ones) and no noise is added to the new incoming points, so the added contribution C is known and deterministic. Fig. 5 presents the distribution of the detection index for three different cases to study the influence of noise. $5 \cdot 10^4$ series are generated to obtain the detection index distribution. The expected value for the limiting case of Fig. 4(b) are reminded with the vertical dashed lines. Fig. 5(a) presents a case where the transition is a sharp step but the following linear increase comprises added noise, with the analytical distribution reminded with the blue solid lines. The expected detection is slightly shifted due to the loss of tidiness in the increasing points but this modification has a limited influence on the distribution of the delay index. Due to the step change at the transition, the order relationship $y_i > y_j, \forall t_i > t_l$ and $t_j < t_l$ is maintained. The added noise has limited impact as long as the step transition remains the main contribution to the tidiness of the series. Second, Figs. 5 (b) and (c) remove the offset at the transition so the immediate following points are not emerging from the initial noise. Figs. 5 (b) and (c) differ in the slope-to-noise ratio, with the slope being respectively 10% and 5% of noise standard deviation. For Fig. 5(b), it

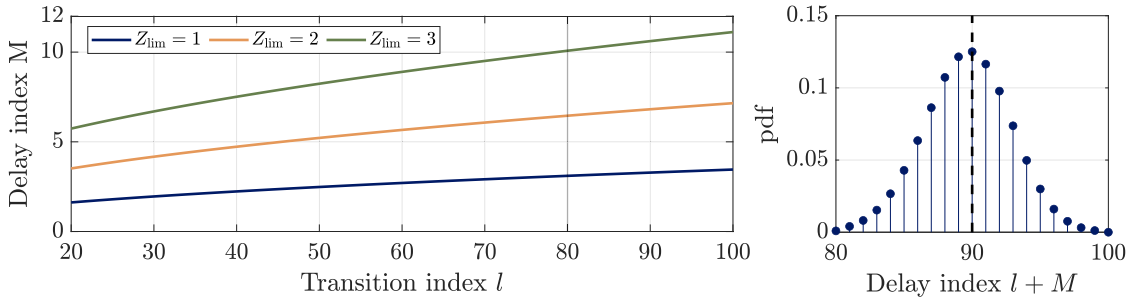

Fig. 4. Reaction to the appearance of a trend. (a) Analytical solution for the expected delay index for the MK-test for confidence $Z_{\text{lim}} = 1$ (blue), $Z_{\text{lim}} = 2$ (yellow), and $Z_{\text{lim}} = 3$ (green) and (b) analytical (blue solid lines) index distribution for the rejection of H_0 with $Z_{\text{lim}} = 3$ for a change at index $l = 80$ (grey), the dashed vertical line corresponds to the analytical solution of (a).

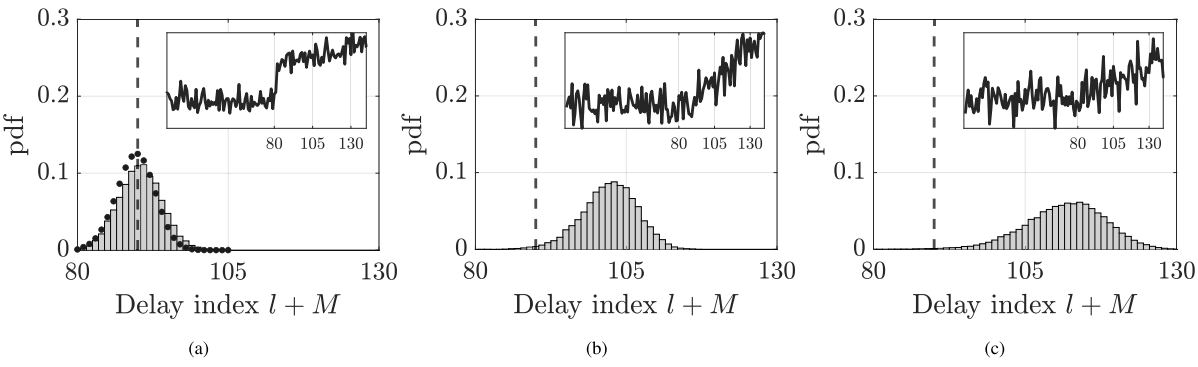

Fig. 5. Empirical index distribution for the rejection of H_0 for a change at index 80 with a confidence of $Z_{\text{lim}} = 3$ (grey) along with the analytical expected transition (vertical dashed lines) for (a) step change with noise, where analytical distribution is reminded in blue solid lines, (b) increasing trend with noise 10% SNR, and (c) increasing trend with noise 5% SNR.

means that $\frac{d\mathbb{E}(y_i)}{dt_i} = 0.1\sigma_N$, where σ_N is the noise standard deviation. The added contribution C is not deterministic anymore, with a delayed and more dispersed detection for lower slope-to-noise ratio due to the loss of structure in the incoming data. As a rule of thumb, the delay modified by the slope-to-noise ratio corresponds to the time needed for a structure to emerge from the noise.

These results are not to be generalised since the delay is mainly case-dependent. However, the main goal here was to remind that the performance of this test is mainly relying on the rank structure of the series, regardless of the actual amplitude of the phenomena. While the MK test alleviates the issues of choosing the learning set of parametric methods, the length of the observation window proved to be a key parameter. The theoretical considerations on the influence of the length of the observation window can help the design of condition monitoring strategies. In online monitoring, the size of available observations is usually growing with two possible strategies: either a sliding observation window with a fixed length or a fixed starting observation point with increasing length. The later strategy has been preferred in this work for its ability to detect long term increases and its suitability for the early detection problem. Yet, the insights gained from the increasing window strategy benefits the sliding one. It sheds light on the compromise between detection confidence and delay, for the choice of an appropriate observation window and gives insight into the obtained values of Z-score in practice.

2.4. Comparison with other methods

The presented work will not expand on the comparison between rank-based and the traditional parametric method for the early detection problem but focus on the benefits of rank-based techniques. Having different initial hypotheses and goals, each method is efficient in its area of design and the duality between the two approaches must be kept. One can present synthetic numeric cases where both frameworks alternatively outperform the other.

For example, in the synthetic example of Fig. 6, the Shewhart control chart [39] (as cited in [40]) change detection algorithm is compared with the Mann–Kendall test. The Shewhart control chart for a change in mean sets the alarm for

$$y_i \geq \overline{y}_J + \kappa \hat{s}_J, \tag{12}$$

where $\overline{y}_J$ and $\kappa\hat{s}_J$ are respectively the centre line and the control limit. Here, these two parameters are chosen as the sample mean and variance estimated over the first J points, where the series is hypothesised stationary, $\overline{y}_J = \frac{1}{J}\sum_{j=1}^{J} y_j$ and $\hat{s}_J =$

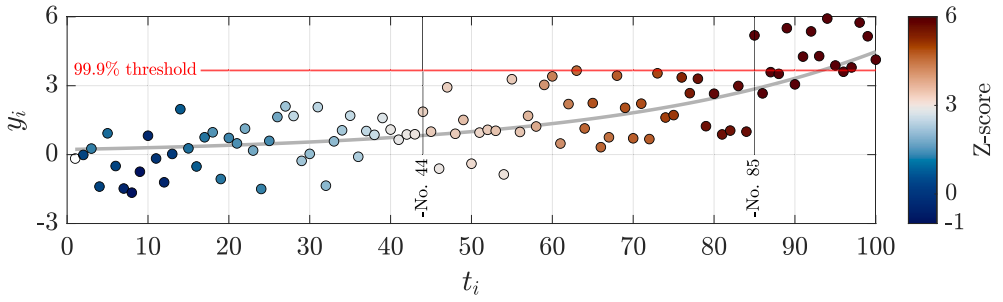

Fig. 6. Test series with hidden exponential trend, $y_i = \exp\{1.5(i-50)/50\} + \epsilon_i$, where ϵ_i is a Gaussian noise with unit variance and the colour of point i stands for the Z-score of series $y_1, \dots, y_i$. For a confidence of 99.9% on the rejection of H_0, the thresholds are indicated by the white transition in the colour map for the MK test, and the red horizontal line for the Shewhart test. The first detection indices for the rejection of H_0 are indicated by the black vertical lines.

$\sqrt{\frac{1}{J-1}\sum_{j=1}^{J}(y_j - \bar{y}_J)^2}$ and the threshold κ is a tuning parameter. Assuming a Gaussian distribution of the noise, the threshold κ can be tuned with a $1-\alpha$ confidence using the properties of the Student's t distribution function. The series of Fig. 6 is sampled from the exponential $y_i = \exp\{1.5(i-50)/50\} + \epsilon_i$ buried within ϵ_i a Gaussian noise of unit variance, where the exponential trend is reminded by grey solid lines. The i^{th} point is coloured according to the Z-score of series $y_1, \dots, y_i$, where the transition between blue and red shades in colourmap corresponds to a 99.9% confidence on the rejection of H_0. Similarly, the change detection algorithm rejects the H_0 hypothesis of whether a point is considered an outlier with a 99.9% confidence assuming a Gaussian distribution of the data. The sample statistics are estimated on the first $J = 33$ samples. The upper control limit for the Shewhart test is shown with red horizontal line in Fig. 6. For an identical confidence of 99.9%, the rejection happens on point 85 for the Shewhart test and 44 for the MK test. The rank-based test outperforms the Shewhart test for these configurations of small increasing trends. While extremely case-dependent for early detection, it is our opinion that both frameworks will eventually detect a change in the system. A slowly increasing trend of an indicator will ineluctably exceed an amplitude-based parametric threshold. On the other hand, a brutal change in the amplitude, easily detectable by a parametric threshold, will eventually create a series ordered enough to reject the H_0 hypothesis.

2.5. Precaution in a context of condition monitoring

The Mann–Kendall test and its corresponding Z-score give a measure on the rejection of the H_0 hypothesis of an independent and identically distributed time series. The practical interpretation of the acceptance or rejection of the test has been widely used as a test on the presence of a trend and has attractive properties for condition monitoring. However, there are some potential pitfalls that could lead to a misinterpretation of the test. First, as developed in Section 2.3, practical monitoring cases are likely to feature series with partial trends, or step-like transitions. Despite having segments without trend, these changes in the distribution of the data create enough order in the rank structure of the series to reject the H_0 hypothesis. The Z-score depends not only on the observation window, but also on the slope to noise ratio of the increase, as developed in Section 2.3. Finally, to avoid false alarm, the series must satisfy the condition of temporal independence. Although outside the scope of this paper, this problem can be mitigated. One can add a pre-processing step to decorrelate the series to satisfy the temporal independence assumption [41] or take into account the lag coefficients to correct for variance [22,34,38].

2.6. Intermediate conclusion

Rank-based statistics provide an interesting framework for condition monitoring. The original aspect is that a developing fault is expected to introduce a positive trend in series of condition indicators. In this section, the Mann–Kendall test has been introduced, illustrated on numerical cases and its ability to detect changes in a series of data explored. This didactic section is not a pledge to favour trend over amplitude-based monitoring but rather an illustrated introduction on these rank-based tools. In what follows, a focus will be made on the Z-score for its ability to summarise the tidiness of a series in a single scalar. The Z-score in itself shows good properties for a trend indicator: insensitivity to outliers, correlated with rank structure of the series, asymptotically unbounded and independent on amplitude.

3. Presentation of the data

3.1. Industrial context

Different tools built on rank-based methods will be presented afterwards. Due to the lack of generalisable degradation models for the vibrations generated by damaged bearings, simulated signals will not be used for the construction of these methods. The illustration of these methods will rely on data collected from industrial wind turbines of the company Engie Green. The database consists of series of run-to-failure industrial vibration signals. The signals were acquired from operating machines with non-stationary

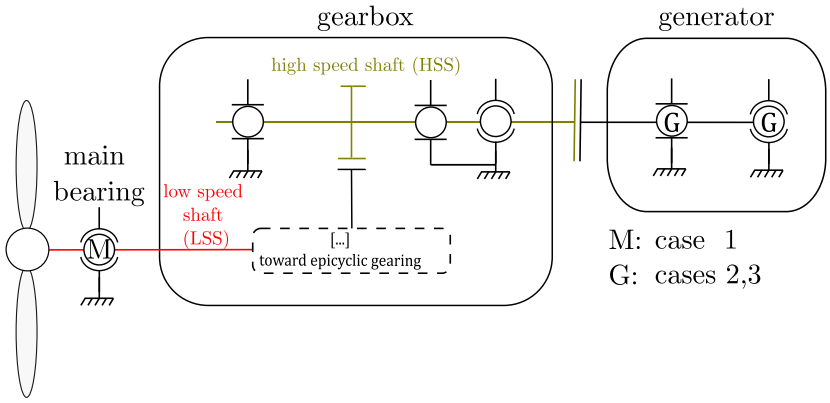

Fig. 7. Schematic representation of the wind turbine shaft line.

Table 1
Illustrating cases. The angle fault frequencies are indicated with respect to the rotation of the inner ring.

Case	#1	#2	#3
Localisation	Main bearing (M)	Generator (B)	Generator (B)
Type	NTN 240/710	SKF 6330	SKF 6330
Inner race	/	1 advanced spall	Multiple spalls
Outer race	Damaged	/	Multiple spalls
Rolling elements	/	/	5 damaged RE
BPFI [epr]	16.3176	5.41	5.41
BPFO [epr]	13.6824	3.59	3.59
BSF [epr]	5.5638	2.365	2.365
FTF [epr]	0.4561	0.399	0.399

load and speed conditions, where the recordings were long enough to allow a frequency analysis. The machines' shaft lines are monitored with fault-sensitive indicators calculated from vibration signals recorded from several accelerometers placed in the vicinity of the bearings. Fig. 7 presents a schematic view of the shaft line of the wind turbines. The input of the gearbox is usually called the low-speed shaft (LSS) and the output the high-speed shaft (HSS), with a gear ratio between the two exceeding a hundred. The gearbox and the generator are separated by a composite coupling. The data used in the following will rely on series of vibration signals recorded from different machines with identified faults. At the end of each series, the damaged bearing was replaced during maintenance operation and accessible to expertise.

For each series of vibration signal, the proposed methods will focus on the evolution of their spectral content. A uniform framework for the processing will be proposed. For the informative frequency band selection of Section 4, a classical discrete Fourier transform is applied on the raw vibration signal. Concerning Hilbert envelope analysis of Section 5, the signal is filtered with a 10th order Butterworth band-pass filter where the demodulation band will be precised in each case. Angle frequency spectra will take the high-speed shaft rotation as the cycle of reference. The generator produces a harmonic signature at $f_g = 72 f_{\mathrm{HSS}}$ and the gear meshing at $f_m = 32 f_{\mathrm{HSS}}$, whose phases, demodulated by narrow-band filtering [42], will be used for angular resampling. The computed angular resampling frequency is 900 events per revolution (epr) of high-speed shaft, chosen to comply with the Nyquist–Shannon sampling theorem.

3.2. Presentation of the cases

Three cases of damaged rolling elements bearings will illustrate the proposed signal processing tools and are summed up in Table 1. The first bearing is located in the low-speed shaft and labelled *M* in Fig. 7. This bearing is a spherical bearing NTN 240/710. The case #1 will deal with the run-to-failure analysis of this bearing. The generator contains two identical 6330 SKF deep-groove ball bearings supporting the high-speed shaft labelled *G* in Fig. 7. The fault frequencies for the two bearings are summed up in Table 1. Fig. 8 presents a close-up view of the inner race faults of cases #1 and #2.

3.3. Precautions regarding the influence of concurrent variations

The following sections present signal processing tools based on trend analysis of signal characteristics. In order to interpret the results for condition monitoring, precautions must be taken to ensure that the long-term evolution is not caused by environmental and/or operational variations (EOVs). The vibration characteristics are not only sensitive to faults, but can also be affected by other concurrent causes such as applied load, speed, lubrication, changes in transmission path or temperature. All these variables cause the

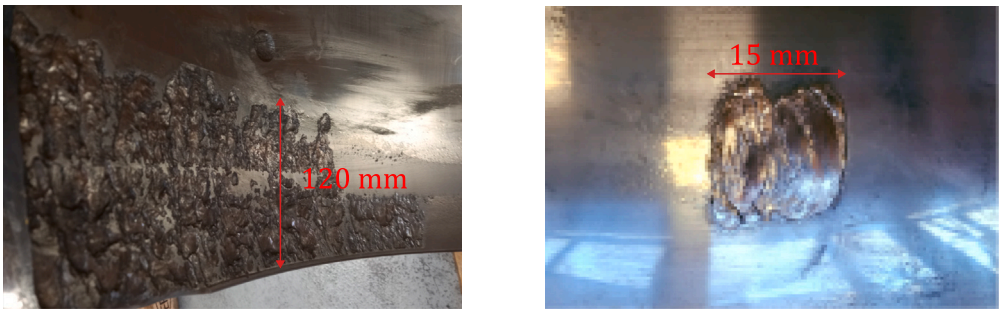

(a) (b)

Fig. 8. Close-up view of the damaged outer race for case #1 (a) and the inner race of case #2 (b).

values of the characteristics to vary from one measurement to another, even when the machine condition is stable. In the industrial application presented here, the active power of the wind turbine during the acquisition encompasses most of the possible concurrent causes.

Ignoring external variables can lead to two main limitations. First, taking signals into account in an undifferentiated way is likely to induce a greater dispersion of the vibration features. A slowly evolving fault is likely to be buried in noise for a longer period of time when the full range of operating conditions is considered. As such, not having a strategy regarding the EOVs amounts to accepting a less favourable noise-to-slope ratio and degraded diagnostic capabilities, as described in Section 2.3. Another possible problem is a change in the distribution of the EOVs, which may induce a trend that is decorrelated with a fault. For example, the average wind speed is higher in winter, with more high power vibration signals recorded, which are expected to have higher amplitude vibration features.

Several strategies can be used to mitigate the influence of EOVs, such as cointegration analysis [43,44], normalisation with regression [45], or analysis of series of signals selected from binned categories of environmental and/or operational conditions [46]. Since this work is not aimed at selecting the best way to mitigate this issue, a simple binning approach is maintained: the procedure is applied to the signal obtained under similar load conditions. This operating variable, highly correlated with the machine speed, proved to explain most of the variability of the condition indicators [45]. This simple approach allows both a reduction in the dispersion of the vibration characteristics and robustness to seasonal variations. Due to the unpredictable operating conditions inherent in the wind energy field, the time interval between each vibration signal is not constant. In the following work, the series will have the index of the recorded signal as the X-axis, where the series are ordered chronologically.

4. Signal processing tool I: the mannagram

4.1. Definition

An incipient fault will introduce changes in the vibrations emitted by the operating machine. However it is well known, especially for the train of impulses generated by a faulty bearing, that the signature is enhanced in specific frequency bands. Mainly, this signature is enhanced around the structural resonances of the system where the signal-to-noise ratio is favourable. Determining these particular frequency bands is precious for diagnosis. These bands are preferred for envelope analysis and integration of bi-spectral representations [16,47]. During the past decade, scholars have focused on numerous methods to guide the choice of an appropriate informative frequency band by detecting and localising it in the frequency domain with the help of fault-sensitive features. Based on the comprehension of vibrations generated by faulty bearings, Antoni proposed to use the spectral kurtosis to track the impulsiveness in the frequency domain [48]. However, the exploration of the whole space of central frequencies and bandwidths is computationally expensive and led Antoni to simplify the tested filter-bank as a binary–ternary decomposition, with the introduction of the fast Kurtogram [49]. The Kurtogram is an appealing concise graphic representation of the spectral kurtosis in multiple frequency bands. Following this work, various methods proposed alternative indicators to explore an exhaustive set of frequency bands using the dyadic decomposition. Since the spectral kurtosis approach may fail under the presence of strong non-Gaussian noise, Barszcz and Jablonski [50] proposed the Protrugram, using the kurtosis of the envelope spectrum as a metric. Lei et al. [51] improved the Kurtogram by using a wavelet packet transform instead of Fourier to enhance transient on noisy signals. Tse and Wang [52] used the L_2L_1 sparsity metric based on wavelet-packet to create the Sparsogram, and Hou et al. [53] used the Gini index as a sparsity measure to highlight the favourable frequency band. Antoni [54] proposed the Infogram by measuring the negentropy of the squared envelope and square envelope spectrum to detect repetitive transients. Moshrefzadeh and Fasana [55] took advantage of the cyclostationarity of bearing fault signals to propose the Autogram based on the kurtosis of unbiased autocorrelation of squared demodulated envelope. The works of Mauricio et al. [56] proposed to pinpoint the optimal frequency band by measuring the emergence of spectral peaks for different integration band of cyclic bi-spectral maps. All these techniques rely on the analysis of a single vibration signal. From the diagnosis point of view, spectral condition indicators are often consequently built on the basis of an informative band pointed by a $-gram$ on a single signal.

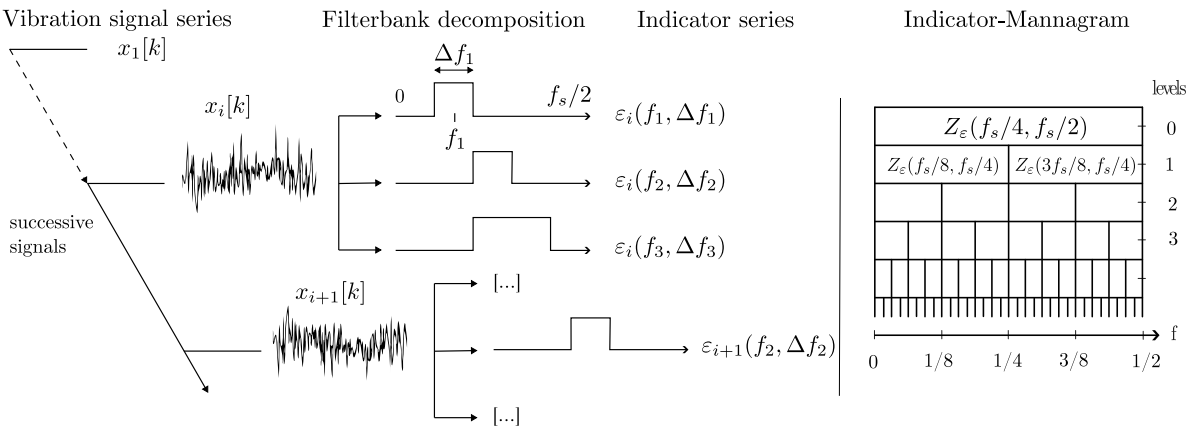

Fig. 9. Illustration of the concept of the mannagram.

If consecutive vibration signals are recorded, each frequency band defined by the dyadic decomposition yields a series of indicators whose trends can be analysed. The frequency band where the fault signature is enhanced is likely to show an increase of the fault sensitive metrics investigated by the $-gram$ approaches such as spectral kurtosis, RMS, sparsity measure, ... etc. The approach proposes to summarise the trend information of a series of dyadic $-gram$ representations using the MK test. Monitoring the increase rather than the amplitude of indicator is likely to give better robustness for incipient fault with less interference from other masking sources. The statistical confidence given by the Z-score is independent on the actual amplitude of the metric, so more generalisable to a fleet of machines.

Formally, one can consider a series of $i = 1, \dots, I$ discrete-time signals, $x_i[k]$, $k = 0, \dots, K-1$ and let $x_i(k, f, \Delta f)$ be the signal filtered in the frequency band $[f - \Delta f/2; f + \Delta f/2]$. For each dyadic filter characteristic $(f, \Delta f)$, a fault-sensitive metric $\varepsilon_i(f, \Delta f)$ can be evaluated within the band. As such, the series of I vibration signals yields multiple condition indicator series, each of it corresponding to a particular frequency band fixed by the dyadic decomposition as shown in Fig. 9. On these several series $\varepsilon_i(f, \Delta f)$, $i = 1, \dots, I$, rank-based statistics can be calculated. The proposed strategy is to display the Z-score of the sum variable $S_\varepsilon(f, \Delta f)$ defined in Eq. (5). The corresponding Z-score $Z_\varepsilon(f, \Delta f)$ will reflect the distance from the H_0 hypothesis, and will be displayed as an image in the $(f, \Delta f)$ plane. This representation defines the *ε-mannagram* as a concise representation of increasing trend of the metric ε in different frequency bands for a given series of vibration signals.

Any metric used in the existing $-gram$ approaches can be used as an input to a mannagram since the diagnosis is made by the increase in the metric rather than its maximal amplitude. Although *-grams* have evolved to fill the gaps left by previous approaches, each with their own specific feature, no -gram is immune to a signal where an external source pollutes the chosen metric. The main idea is to combine the power of the fault-sensitive metric with its necessary increase with the appearance of the fault. The following section presents a first illustration on a difficult case for a kurtogram analysis. In addition to the spectral kurtosis (SK), a second illustration will be made on the evolution of vibration energy of signal filtered in different frequency bands with the root mean square (RMS) mannagram.

4.2. Applications

4.2.1. A demodulation band selection tool, illustration on case #1

The benefits of focusing on the trend of series of *-grams* are illustrated on the case #1. This example concerns a defective main bearing, located on the low-speed shaft at the input of the gearbox. The bearing was monitored for approximately one year, giving a series of 50 vibrations signals $\{x_1, \dots, x_{50}\}$. The bearing was replaced during a maintenance operation and presented a badly damaged outer race. Despite the severity of the damage, this case was difficult to diagnose and monitor. This bearing operates at low speeds (15–20 rpm), with a weak vibration fault signature compared to concurrent sources. The envelope analysis is preferred for diagnosis, but comes up against the selection of an appropriate frequency band. Fig. 10 compares the frequency bands indicated by the kurtograms (top) and the kurto-mannagrams (bottom), their trend-based counterparts. A kurtogram was calculated for each signal, with the band of maximal spectral kurtosis summed up in Fig. 10 (top). The highest spectral kurtosis seems to be almost consistently located in the $[0; 1250]$ Hz band, with values of spectral kurtosis below 0.5. Some signals stand values of spectral kurtosis higher than one, clipped by the colour map limits.

Mannagrams are then calculated progressively by extending chronologically the series: the ith mannagram takes into account the first i kurtograms $x_1, \dots, x_i$. The series of spectral kurtosis in each band are concatenated with the Z-score, giving synthetic information about the trend in each frequency band. The bands with the maximal Z-score are shown in Fig. 10 (bottom). The interpretation of bands at the beginning of the series should be interpreted with caution since no trend has stabilised. However, from the 30th signal onwards, the band stabilises at $[1250; 1562.5]$ Hz, with increasing confidence in the presence of a trend as indicated by the growing Z-score.

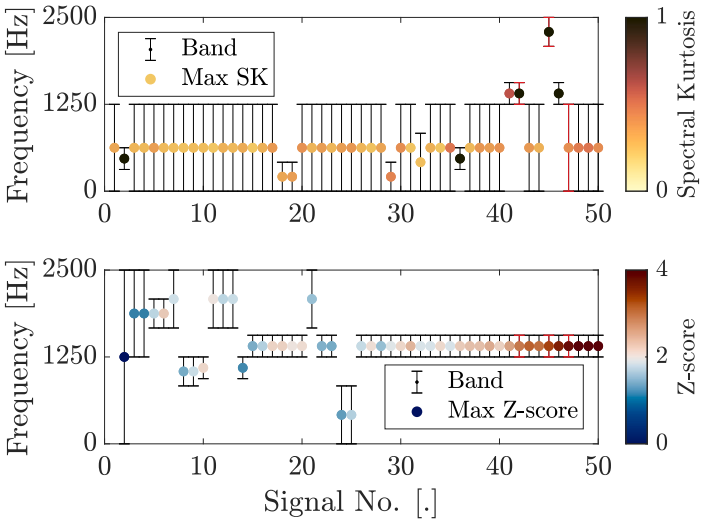

Fig. 10. Case #1: Bands of maximal metric given by the kurtogram (top) with maximal spectral kurtosis, and kurto-mannagram (bottom) with maximal Z-score. Points investigated later are highlighted in red.

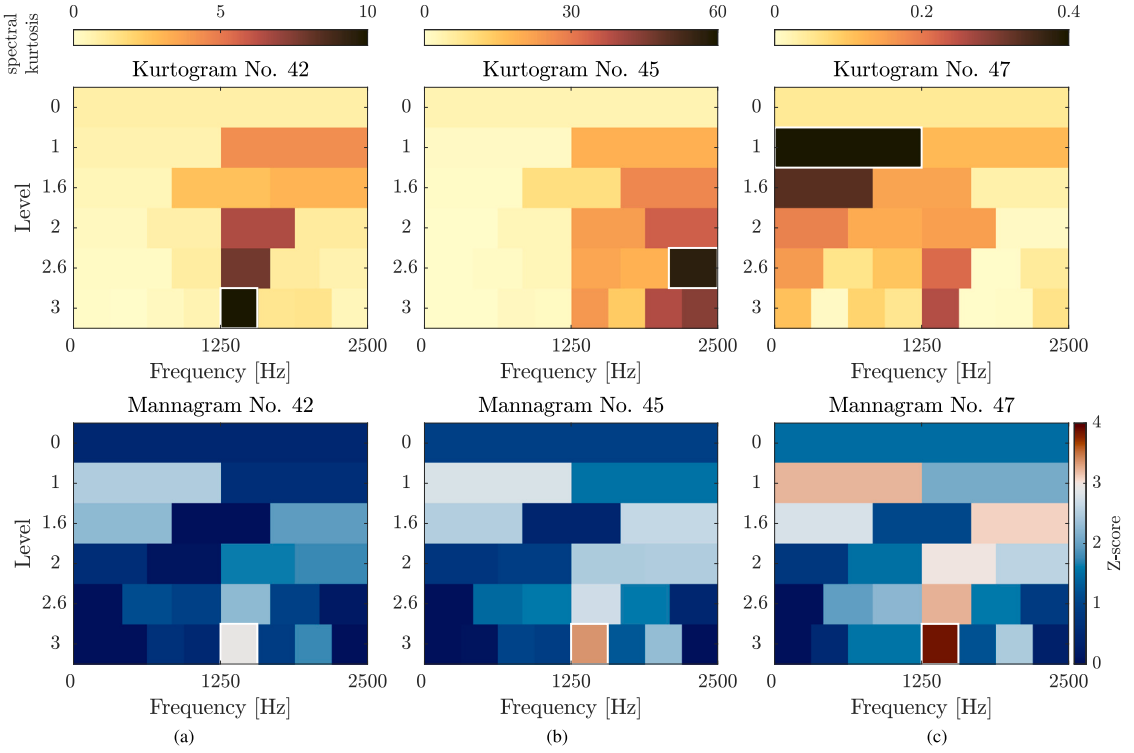

Fig. 11. Case #1: comparison of kurtograms (top) and their trend-based counterparts Kurto-mannagrams (bottom). Kurtograms of signals No. 42 (a), 45 (b), and 47 (c) are compared to the mannagrams of the corresponding series, series No. 42 ($i = 1, \dots, 42$) (a), series No. 45 ($i = 1, \dots, 45$) (b) and series No. 47 ($i = 1, \dots, 47$) (c). The band of maximal metric is highlighted by a white rectangle for each subfigure. The scale of the colourmap is indicated above for the kurtograms and is shared for all the mannagrams.

Fig. 11 compares the kurtograms (top) of the signals 42, 45, and 49 with the kurto-mannagrams of the corresponding series $x_1, \dots, x_i$ (bottom). The colour map for each kurtogram is shown above, while the colour map for the mannagrams is shared and shown on the right. Some frequency bands have a non-significant negative Z-score, hidden by the choice of the colour scale to focus on increasing trends. The bands of maximum spectral kurtosis (top) and maximal Z-score (bottom) are highlighted by white rectangles. The amplitude of the spectral kurtosis varies greatly for the three signals, indicating three different frequency bands.

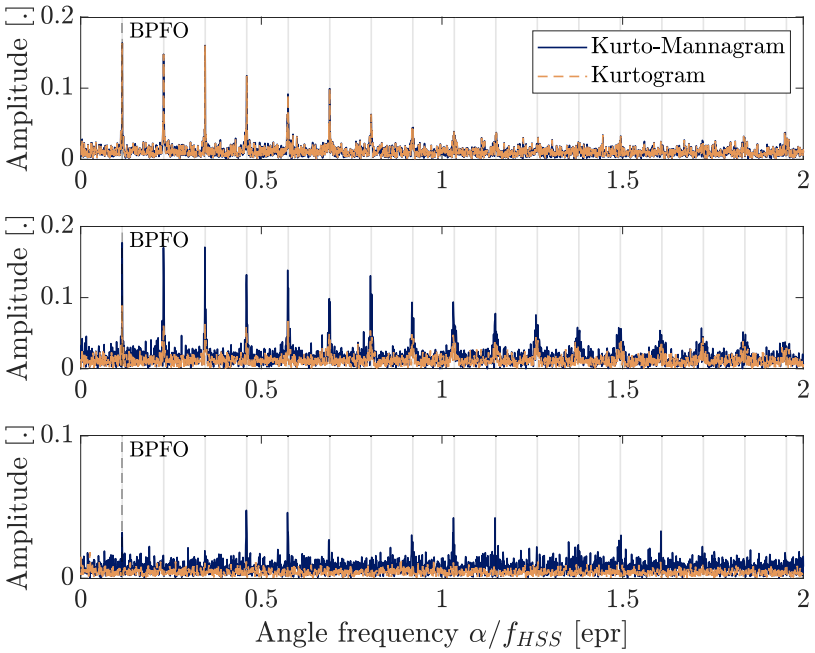

Fig. 12. Case #1: Envelope spectra of vibration signals No. 42 (up), No. 45 (middle) and No. 47 (bottom) zoomed around the first harmonics of the BPFO, for different demodulation frequency bands. The envelope spectra with the frequency bands pointed out by the mannagrams are indicated in blue, and in yellow for the kurtograms.

On the other hand, the mannagrams steadily highlight the $[1250; 1562, 5]$ Hz band, with growing confidence on the presence of the trend.

Fig. 12 presents the envelope spectra of signals 42 (top), 45 (middle) and 47 (bottom), bandpass filtered prior to the Hilbert transform in the band $[1250; 1562, 5]$ Hz indicated by the mannagram approach (blue lines), or in the band indicated by the kurtogram (yellow dashed lines). On top subfigure, the two approaches highlight the same $[1250; 1562, 5]$ Hz band, where the spectral signature of the defect is seen by the peak comb at the fault frequency. This signal is a favourable case for the kurtogram, where the fault signature is impulsive enough to outweigh other interfering sources. In the light of Fig. 10, this situation occurred only 3 times in the series and should correspond to conditions where the defect signal-to-noise ratio was particularly favourable. The mannagram approach is in agreement and points towards the same band. In the middle subfigure, the signal was probably polluted by a highly impulsive source ($\max SK = 60$ in Fig. 11 (top-b)) and pointed towards the $[2083; 2500]$ Hz band. The mannagram is not affected by this outlier and shows a more favourable band compared to the kurtogram with increased amplitude of the BPFO peaks. Finally, for the signal 47 in the bottom subfigure, the kurtogram indicates the $[0; 1250]$ Hz band, in line with the majority of signals in the series of Fig. 10 (top). The kurtogram performs poorly here, where the fault signature disappears compared to the mannagram band.

Obviously, the case study is unfavourable for kurtogram analysis, with a defect generating a weak impulsivity, polluted by interfering sources, and whose visibility varies from one signal to another. However, the long-term increase in impulsivity is captured by the trend analysis, which provides a robust and consistent solution to the issue of informative band selection. The choice of the kurtogram was made for illustrative purposes. Other *-grams* might have worked better in this case. However, regardless of the metric, one can always consider a worst-case scenario where polluting sources will hinder the analysis, and where the benefits of trend-based techniques will provide additional help in the selection of an informative band.

4.2.2. *Favourable indicators for fault trending, illustration on case #2*

On the top of being good a candidate to the demodulation problem, the mannagram points out interesting frequency bands for fault severity trending. Indeed, the frequency bands where the H_0 hypothesis is rejected likely indicates areas where the SNR is high, yielding new series of indicators. In the light of fault signature enhancement around the informative band, monitoring the vibration energy with the RMS of the band-pass filtered signal is expected to be well-suited for rank analysis. Indeed, due to a favourable signal-to-noise ratio (SNR), one can expect an early and well-ordered increasing trend of the RMS in these frequency bands. It thus makes sense to test the hypothesis of an increasing trend of vibration energy in exhaustive set of frequency bands. For each dyadic filter characteristic $(f, \Delta f)$, the vibration energy metric $\varepsilon_i(f, \Delta f)$ within the band is

$$\varepsilon_i(f, \Delta f) = \sqrt{\frac{1}{K} \sum_{k=0}^{K-1} |x_i(k, f, \Delta f)|^2}. \tag{13}$$

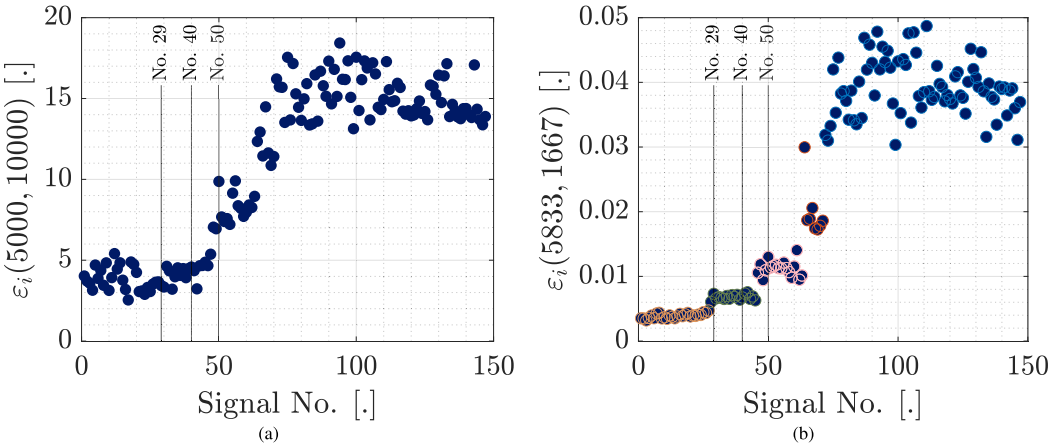

Fig. 13. Series of RMS for the case #2, for the global RMS in the band $[0; 10000]$ Hz ($f = 5$ kHz, $\Delta f = 10$ kHz) (a) and in the band $[5000; 6667]$ Hz ($f = 5833$ Hz, $\Delta f = 1667$ Hz) (b). The later band is pointed out by the Mannagram approach and a proposed segmentation of the series is indicated by the contour colours. For both subfigures, points investigated are indicated by vertical lines.

As such, the series of I vibration signals yields multiple filtered vibration energy series, each of it corresponding to a particular frequency band fixed by the dyadic decomposition.

To illustrate this point, the case #2 of the faulty bearings of Section 3 will be investigated. This bearing was closely monitored during 6 months giving a series of vibration signals x_i. At the end of the monitoring period, the bearing was replaced, and a unique spall was found on the inner race. As shown in Fig. 8, the spall was in an advanced stage of degradation. Fig. 13(a), presents the series of global RMS level of each signal x_i.

Fig. 14 selects the RMS-mannagrams of series No. 29, 40 and 50 for further investigation. Fig. 14(a) shows the Mannagram for the series No. 29, chosen to highlight the first area to exceed the threshold of $Z_{lim} = 4$. The corresponding band at decomposition level 2.6 is $[5000; 6667]$ Hz for $Z = 4.28$. Comparatively, the global RMS level corresponding to the level 0, has a Z-score equal to $Z = 2.06$, which is not enough to reject the H_0 hypothesis under the chosen confidence limit. Fig. 14(b) presents the Mannagram for the series No. 29, corresponding to a threshold crossing for the level 0 global RMS series. The frequency band $[5000; 6667]$ Hz is still showing the greatest Z-score equal to 6.20. Yet, the fault signature is now energetic enough to produce ordered series in other frequency bands shown in shades of red. Fig. 14(c) shows the Mannagram for the series No. 50, chosen quantitatively for a visual change in the global RMS series. All the previous trends on frequency bands are confirmed, with still a highlighted band between $[5000; 6667]$ Hz. Complementary, the Z-score series of filtered RMS for the bands $[0; 10000]$ Hz (blue) and $[5000; 6667]$ Hz (yellow) are shown in Fig. 15. The threshold of $Z_{lim} = 4$ on the rejection of H_0 is represented by the red horizontal line. During the first 10 points, the Z-score series distribute randomly within the $\pm 3\sigma_{S_0}$ area, in agreement with the theoretical developments of Section 2 for a series with no initial trend. Concerning the global RMS series shown in blue, the first series to exceed the threshold of $Z_{lim} = 4$ is confirmed to be the series No. 40 $x_1, \ldots, x_{40}$, as previously shown by the Mannagram of Fig. 14(b). Towards the end of the observations, the Z-score series are slightly decreasing in agreement with the negative slope observed in Fig. 13(a). One explanation could be the mechanical lapping of the spalled area, reducing the vibration energy released by the interaction between rolling elements and the spall. Comparatively, the Z-score series for the frequency band pointed out by the Mannagram reacts earlier with a threshold crossing for the series No. 29 $x_1, \ldots, x_{29}$. In the view of Fig. 13(a), it is clear that the rejection of H_0 with amplitude-based methods would have been triggered later, roughly near index 50.

Not only the Mannagram permits an earlier alarm on the appearance of a fault in the system, but the corresponding filtered RMS series provides more information about the fault evolution. Fig. 13(b) presents the series ε_i of energy level corresponding to the frequency band previously highlighted by the Mannagrams of Fig. 14. The detection indices of Fig. 15 are shown with the black vertical lines. Comparatively with the global RMS series of Fig. 13(a), the filtered RMS series pointed out by the Mannagram shows appealing properties for both fault detection and trending. First, concerning the first portion of the series, the energy level seems less dispersed than the RMS around the mean value, possibly because the frequency band is characterised by a favourable signal-to-noise ratio. Unlike Fig. 13(a), a clear step change is observed around signal No. 29 possibly localising more precisely the date on which the fault appeared in the bearing.

Further, the series unveils different step sections as opposed to the previous sigmoid shape. Qualitative clusters of the series are proposed in Fig. 13(b) with different edge colours. Qualitatively, there is a first section between signals 1 to 27 (yellow edge). A first stage of the fault is then visible from signal 28 to 45 (green edge). Additional transitions can be seen from signals 46 to 63 (pink edge), 64 to 71 (red edge) and after signal 72 (light blue edge). The piecewise constant shape of the vibration energy series appears more interpretable regarding a degradation process due to sub-surface initiated fatigue. As studied by the tribology community, subsurface initiated fatigue is due to micro-cracks that propagate below the raceway surface [57–59]. The crack eventually grows to a critical length, and reaches the raceway while the corresponding flake is peeling of the surface. From this pit, new cracks may

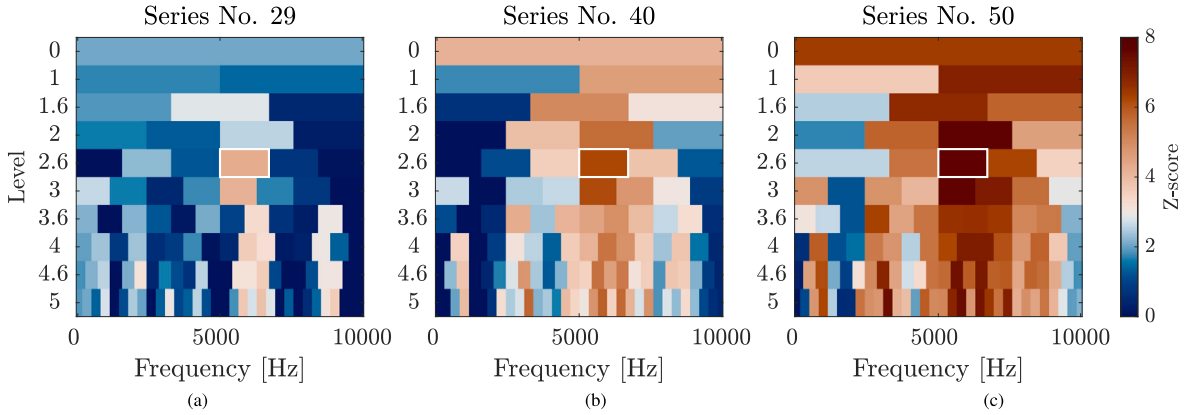

Fig. 14. RMS-Mannagrams of the series No. 29 ($i = 1, \dots, 29$) (a), series No. 40 ($i = 1, \dots, 40$) (b) and series No. 50 ($i = 1, \dots, 50$) (c) for the case #2. The scale of the colourmap is identical for each sub-figure.

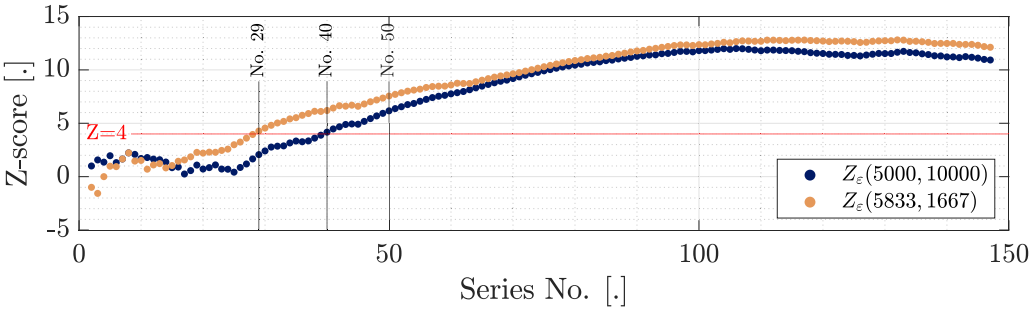

Fig. 15. Z-score of RMS series in the band [0; 10000] Hz ($f = 5$ kHz, $\Delta f = 10$ kHz) (blue) and in the band [5000; 6667] Hz ($f = 5833$ Hz, $\Delta f = 1667$ Hz) (yellow) for the case #2. Points investigated are indicated by vertical lines.

develop extending the spalled area displaying a V-shape. Fig. 8 (b) shows the scaled surface texture of the fault on bearing #2. These phenomena of material removal are sudden and are expected to induce step-like changes in the vibration levels if the inter-time acquisition between two signals is short enough. The hypothesis of this work is that investigating frequency bands with maximal trend characteristics rather than maximal fault-sensitive metric value may uncover insightful piece of information previously hidden by other sources of noise.

4.3. Mannagram conclusion

In this section, a new rank-based tool called the Mannagram has been introduced. Derived from the *-gram* concept, the Mannagram proposes to summarise in a single representation the trend of fault-sensitive metric series stemming from various frequency bands. By accounting for a series of indicators instead of a single one, the focus is made on the monotonous change introduced by the fault rather than the maximum value. Cases where the fault sensitive feature, such as the kurtosis, is covered by other sources in the signal can be handled since the interference will be stationary for the different recorded signals. While the principle could be extended to other fault indicators, monitoring the vibration energy with filtered RMS series showed good severity trending properties.

5. Signal processing tool II: the Kendrum

5.1. Definition

When investigating a signal recorded from a machine to be diagnosed, most of the time it comes down to the interpretation of a 1D spectral representation. Due to the cyclostationary properties of the fault signature, it is characterised by peaks located on specific angular frequency bins. Different spectral representations coexist such as the spectra of raw or envelope signal, integrated cyclic coherence, or integrated order-frequency spectral coherence, coming from vibration or instantaneous angular speed measurements. In any case, a sole spectral representation may be difficult to interpret with a high level of confidence on the presence of a fault. The spectral representations can be extremely rich with numerous peaks normally found in the healthy state. As a consequence, most of

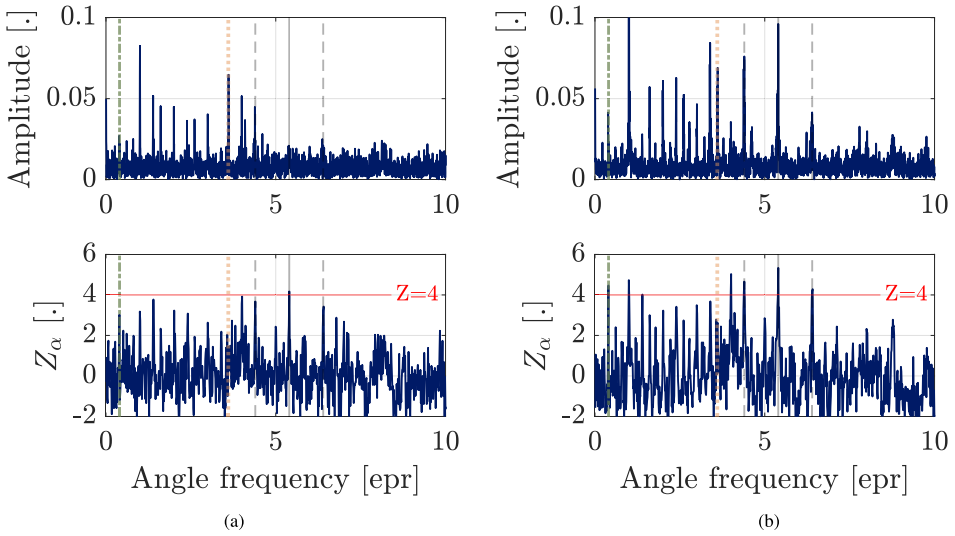

Fig. 16. Envelope spectrum (top) and envelope kendrum (bottom) for signals (respectively series) (a) No. 24 and (b) No. 29. The vertical lines represent the bearing fault frequencies BPFI (square grey solid lines), modulations sidebands BPFI ±1 (square grey dashed lines), BPFO (diamonds yellow dotted lines) and FTF (circle green dot–dash lines).

the time diagnosis is done with a comparison to a reference state. Randall developed a constant percentage bandwidth reference and studied the difference between two spectra to detect abnormal changes [60,61]. The method was used on the monitoring of a gas-turbine pump [62]. When comparing three or more spectral representations, it is likely to fall down to waterfall 3D representations, difficult to handle.

The properties of the MK test Z-score can thus be used to summarise multiple chronological spectra into a single 1D representation. Formally, one can consider a series of $i = 1, \dots, I$ discrete spectra $X_i[\alpha_k]$, where the indices i are ranked chronologically and α_k is the central cyclic frequency for the bin k. Each bin α_k defines a series $X_i[\alpha_k]$ on the index i on which the MK-test can be applied, and the corresponding Z-score $Z_\alpha(\alpha_k)$ on the rejection of the hypothesis of H_0 calculated. The corresponding representation presents the Z-score for each frequency bin for a series of I signals. The authors propose to define the kendrum as the summarising representation of changes in a series of 1D spectral representation.

Even if the concept can be extended to summarise other series of spectra, the following applications will focus on series of envelope spectra with angular resampling with respect to a rotation of reference. A pre-whitening operation to remove the influence of the structure may reduce the variability in the spectrum due to different rotating speed conditions.

5.2. Applications

5.2.1. An investigation tool, illustration on case #2

The method is applied on the series of vibration signals of case #2. The signal is band-passed on the frequency band previously highlighted by the Mannagram. The first angular frequency bin to exceed $Z = 4$ has a central frequency of $\alpha_k = 5.397$ epr for signal No. 24, only 5 indices before the Mannagram-aided detection. Fig. 16 presents the envelope spectra and the corresponding Z-score for indices 24 and 29. In the envelope spectrum of signal No. 24, the most prominent fault peak was located at the BPFO, with barely noticeable contributions of the BPFI peak and the modulations sidebands. However, the corresponding envelope kendrum shows that the Z-score of the BPFI bin exceeds $Z = 4$, indicating with high confidence an early increase of the cyclic energy. On the contrary, the BPFO Z-score indicates that the peak amplitude is stationary despite its prominence on the spectrum. It is known by the maintenance company that generator bearings tend to show peaks at the fault frequencies, even without having visible spalls on the races or rolling elements. While this may at first seem counter-intuitive, the emergence of fault frequencies without localised defects has been studied by Meyer et al. [63]. These trends are confirmed for index 29 of Fig. 16(b), the envelope spectrum permits the identification of a BPFI peak and its modulation sidebands without ambiguity, confirmed by the envelope kendrum. Compared to the envelope spectrum, the envelope kendrum highlights also other frequencies linked to the kinematic of the fault: FTF and shaft harmonics. The increase at such frequencies was less obviously linked to the extension of the fault in the spectrum due to the different relative amplitudes and the presence of other tonal contributions in the spectrum, while the information on the trend is preserved in the kendrum. This additional information may raise the diagnosis confidence.

5.2.2. An experience feedback tool, illustration on case #3

The summarising properties of the Z-score can also be used to visualise the different frequency bins featuring an increasing trend when confronted to a bearing with multiple faults. This piece of information can be useful to understand the link between different

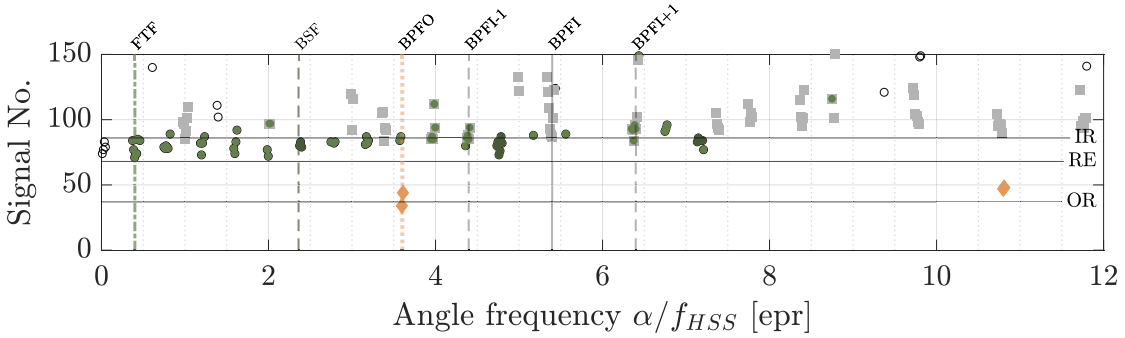

Fig. 17. Trend detection by frequency bin for equalised envelope spectra. Each point represents the index of the first rejection of H_0 for the MK test. The vertical lines indicate the fault frequencies for the FTF (light green dash–dot lines), BSF harmonics (dark green dashed lines), BPFO (dotted yellow lines), BPFI (grey solid lines) and BPFI ±1 shaft modulation (grey dashed lines). Frequency channels with detection of outer race fault frequencies are shown with yellow diamonds, rolling elements in green circles with FTF harmonics (light green) and BSF harmonics (dark green) and finally, the inner race faults frequencies (BPFI and shaft) in grey squares. The width of the markers is not representative of the bins width.

fault frequencies, when confronted to the systemic degradation of the bearing. Since the kendrum uses only the trend information, other fault frequencies with lower amplitude, usually left away, are magnified. The bearing case #3 presents multiple defects on both races and rolling elements. Fig. 17 presents the index of first rejection of H_0 with the MK test with a confidence corresponding to $Z_{lim} > 3.3$ for each frequency bin of the series of envelope spectra in the band pointed out by the Mannagram approach. The points are coloured according to the expected related fault frequency channel: yellow for the outer race (OR), green for the rolling elements (RE) and grey for the inner race (IR). The frequency channels are associated to a specific fault group by taking a tolerance of ±0.06 epr around the adjusted fault frequency. The fault frequency is adjusted to account for the actual operating kinematic conditions. The operating BPFO is shifted upward by 0.5% of the theoretical fault frequency, and the other fault frequencies are adjusted accordingly. Three groups of frequency channels related to the consecutive developments of faults appear in the figure. The first frequency channels to reject H_0 are shown with the yellow diamonds and correspond to the BPFO fault frequency and its 2nd and 3rd harmonics around the index 40. Then, around the index 70, both the BSF and FTF frequencies shown in green react, indicating the degradation of rolling elements. Finally, around index 85, frequency channels linked to the development of an inner race defect, that is shaft modulated BPFI harmonics and shaft harmonics, reject the H_0 hypothesis. Interestingly, high order sidebands (up to ±3) of the BPFI peaks are unveiled, even with their low relative amplitude compared to the BPFI carrier.

Multiple frequency bins around the expected fault frequency react with a dispersion on the detection index. This can be induced by multiple causes. First, the estimation errors of the shaft angle–time relationship combined to the smearing of the spectral signature caused by the pseudo-cyclostationary nature of bearing fault signals [64] cause the peaks to spill on adjacent bins. These adjacent bins are likely to reject the H_0 hypothesis later since the amplitude increase will be less ordered. Further, as described by Bertoni and André [65], the fault frequencies are expected to drift with the extension of the fault which also explain part of the dispersion around the theoretical values and motivated the tolerance in the label of the fault frequencies. Apart from the mentioned frequency channels, most of the remaining bins comply with the hypothesis of an absence of trend, which permits a clear identification of the degradation without the pollution of other components with strong relative amplitudes.

This concise representation reveals insight into the different phases of the bearing degradation. Cluster of points related to classical fault frequencies react around the same indices. While classical analysis tends to focus on the main fault frequency with a few modulations bands of prominent amplitude, the rank-based analysis equalises other contributions of related sidebands. This effect combined with the disappearance of other non-evolving peaks is likely to increase the level of confidence of the diagnosis. The experience gained from such representation may also help in the design of appropriate health indicators.

5.3. Kendrum conclusion

The summarising properties of the Z-score for the MK test are easily transferable to the monitoring of series of Fourier coefficients from a spectral representation. Here applied to envelope spectrum of a vibration signal, the Kendrum illustrates the long term amplitude trends of each frequency channel with a single scalar. By silencing other stationary frequency channels and highlighting low but increasing amplitude bins, the diagnosis and experience feedback is facilitated.

6. General conclusion

This paper has investigated the benefits of rank-based trend analysis for vibration-based condition monitoring. Namely, the Mann–Kendall test uses the rank association of a series to assess the presence of a trend. An illustrated theoretical background on rank-statistics has been reminded. With the view to monitoring series of condition indicators, results on the appearance of a trend in a series have been explored. The Mann–Kendall test offers a scalar on the presence of a trend, the Z-score, that can be interpreted with statistical confidence. Based on this, new tools for vibration-based condition monitoring have been introduced. Concerning the

informative band selection, the *Mannagram* proposes to concatenate a series of condition indicators filtered with a dyadic filter-bank decomposition by displaying the Z-score for increasing trends in each frequency band. Concerning the spectral analysis, the *Kendrum* summarises the trend analysis of series of spectra by displaying the Z-score for each frequency bin. Both methods have been tested on series of vibration signals recorded from industrial wind turbines with damaged bearings. By focusing on long-term trends, the new tools have shown appealing properties for diagnosis.

The key takeaways are:

- The rank-based Mann–Kendall test detects the presence of a trend in a series. This test is non-parametric and robust to outliers.
- In the form of the Z-score, the Mann–Kendall test offers a robust scalar trend indicator.
- Mechanical faults are likely better detected by the increase rather than the absolute amplitude of a condition indicator.
- A new tool coined the *Mannagram* has been introduced for the informative band selection problem as a summarising representation of the trend of series of $-grams$.
- A new tool coined the *Kendrum* has been introduced to summarise the amplitude trend of multiple frequency bins for a series of spectra.

CRediT authorship contribution statement

Adrien Marsick: Writing – original draft, Software, Methodology, Conceptualization. **Hugo André:** Writing – review & editing, Supervision, Methodology, Conceptualization. **Ilyes Khelf:** Supervision, Resources, Funding acquisition. **Quentin Leclère:** Writing – review & editing, Supervision, Funding acquisition, Conceptualization. **Jérôme Antoni:** Writing – review & editing, Supervision, Conceptualization.

Declaration of competing interest

The authors declare that they have no known competing financial interests or personal relationships that could have appeared to influence the work reported in this paper.

Data availability

The authors do not have permission to share data.

Acknowledgements

This work was supported by the LABEX CeLyA, France (Grant No. ANR-10-LABX-0060) of Universite de Lyon, within the program "Investissements d'Avenir" (Grant No. ANR16-IDEX-0005) operated by the French National Research Agency (ANR). The MATLAB R2021 software was used to implement the methods described in this work.

The scientific colour map *vik* [66] is used in this study to prevent visual distortion of the data and exclusion of readers with colour vision deficiencies [67].

Appendix. Indices derivation

A.1. Exact derivation

In the case of perfectly ordered continuation where all the pairs are concordant, $t_i < t_j, y_i < y_j$, for $i \in [1, l{+}M]$ and $j \in [l{+}1, l{+}M]$, the added contribution C to the sum variable $S(l+M)$ at index $l+M$ is

$$C = \sum_{m=0}^{M-1} (l+m) = Ml + \frac{M(M+1)}{2}, \tag{A.1}$$

and the variance of the Gaussian distribution for H_0 is

$$\sigma^2_{S_0}(l+M) = \frac{(l+M)(l+M-1)(2(l+M)+5)}{18}. \tag{A.2}$$

The detection condition is

$$\mathbb{E}\{Z(l+M)\}^2 = Z^2_{\text{lim}}, \tag{A.3}$$

which yields to

$$\left(Ml + \frac{M(M+1)}{2} - 1\right)^2 - \frac{(l+M)(l+M-1)(2(l+M)+5)}{18} Z^2_{\text{lim}} = 0. \tag{A.4}$$

The expected rejection index M for a transition occurring at index n for a confidence level given by $Z = Z_{\text{lim}}$ is the roots of the polynomial

$$A_4 M^4 + A_3 M^3 + A_2 M^2 + A_1 M + A_0, \tag{A.5}$$

with

$$A_4 = 1 \tag{A.6}$$

$$A_3 = 4\left(l - Z_{\text{lim}}^2/9 + 1/2\right) \tag{A.7}$$

$$A_2 = -4(l(Z_{\text{lim}}^2/3 - 1 - l) + Z_{\text{lim}}^2/6 + 3/4) \tag{A.8}$$

$$A_1 = -4\left(l(2 + Z_{\text{lim}}^2/3(1 + l)) + 1 - Z_{\text{lim}}^2 5/18\right) \tag{A.9}$$

$$A_0 = \frac{2Z_{\text{lim}}^2 l}{9}\left(5 - 3l - 2l^2\right) + 4. \tag{A.10}$$

A.2. Asymptotic analysis

Given an initial window length l way greater than M, Eq. (A.4) yields

$$l^2 M^2 \approx \frac{Z_{\text{lim}}^2}{9}(l + M)^3, \tag{A.11}$$

that gives with further simplification

$$M = O(l^{1/2}). \tag{A.12}$$

References

[1] D.-Y. Kim, H.-B. Yun, S.-M. Yang, W.-T. Kim, D.-P. Hong, Fault diagnosis of ball bearings within rotational machines using the infrared thermography method, J. Korean Soc. Nondestruct. Test. 30 (6) (2010) 558–563, Publisher: The Korean Society for Nondestructive Testing.

[2] J.M. Wakiru, L. Pintelon, P.N. Muchiri, P.K. Chemweno, A review on lubricant condition monitoring information analysis for maintenance decision support, Mech. Syst. Signal Process. 118 (2019) 108–132, http://dx.doi.org/10.1016/j.ymssp.2018.08.039, URL: https://linkinghub.elsevier.com/retrieve/pii/S0888327018305788.

[3] S.M.A. Al-Obaidi, M.S. Leong, R.R. Hamzah, A.M. Abdelrhman, A review of acoustic emission technique for machinery condition monitoring: Defects detection & diagnostic, Appl. Mech. Mater. 229–231 (2012) 1476–1480, http://dx.doi.org/10.4028/www.scientific.net/AMM.229-231.1476, URL: https://www.scientific.net/AMM.229-231.1476.

[4] H. Andre, A. Bourdon, D. Rémond, On the use of the Instantaneous Angular Speed measurement in non-stationary mechanism monitoring, in: ASME 2011 International Design Engineering Technical Conferences, Washington, United States, 2011, pp. DETC2011/MECH–47470, URL: https://hal.archives-ouvertes.fr/hal-00694854.

[5] W.T. Thomson, I. Culbert, Current Signature Analysis for Condition Monitoring of Cage Induction Motors: Industrial Application and Case Histories, John Wiley & Sons, Inc., Hoboken, NJ, USA, 2016, http://dx.doi.org/10.1002/9781119175476, URL: http://doi.wiley.com/10.1002/9781119175476.

[6] R.B. Randall, Vibration-Based Condition Monitoring: Industrial, Aerospace and Automotive Applications, first ed., Wiley, 2011, http://dx.doi.org/10.1002/9780470977668, URL: https://onlinelibrary.wiley.com/doi/book/10.1002/9780470977668.

[7] A. Rai, S.H. Upadhyay, A review on signal processing techniques utilized in the fault diagnosis of rolling element bearings, Tribol. Int. 96 (2016) 289–306, http://dx.doi.org/10.1016/j.triboint.2015.12.037, URL: https://www.sciencedirect.com/science/article/pii/S0301679X15006052.

[8] D. Wang, Some further thoughts about spectral kurtosis, spectral L2/L1 norm, spectral smoothness index and spectral Gini index for characterizing repetitive transients, Mech. Syst. Signal Process. 108 (2018) 360–368, http://dx.doi.org/10.1016/j.ymssp.2018.02.034, URL: https://www.sciencedirect.com/science/article/pii/S0888327018300979.

[9] B. Chen, Y. Cheng, W. Zhang, F. Gu, Investigations on improved Gini indices for bearing fault feature characterization and condition monitoring, Mech. Syst. Signal Process. 176 (2022) 109165, http://dx.doi.org/10.1016/j.ymssp.2022.109165, URL: https://www.sciencedirect.com/science/article/pii/S0888327022003223.

[10] J. Antoni, P. Borghesani, A statistical methodology for the design of condition indicators, Mech. Syst. Signal Process. 114 (2019) 290–327, http://dx.doi.org/10.1016/j.ymssp.2018.05.012, URL: https://www.sciencedirect.com/science/article/pii/S0888327018302632.

[11] P.D. McFadden, J.D. Smith, Model for the vibration produced by a single point defect in a rolling element bearing, J. Sound Vib. 96 (1) (1984) 69–82, http://dx.doi.org/10.1016/0022-460X(84)90595-9, URL: https://www.sciencedirect.com/science/article/pii/0022460X84905959.

[12] G. D'Elia, M. Cocconcelli, R. Rubini, G. Dalpiaz, et al., Evolution of gear condition indicators for diagnostics of planetary gearboxes, in: Proceedings of the International Conference Surveillance 8, FRA, 2015.

[13] C. Peeters, Q. Leclère, J. Antoni, P. Lindahl, J. Donnal, S. Leeb, J. Helsen, Review and comparison of tacholess instantaneous speed estimation methods on experimental vibration data, Mech. Syst. Signal Process. 129 (2019) 407–436, http://dx.doi.org/10.1016/j.ymssp.2019.02.031, URL: https://linkinghub.elsevier.com/retrieve/pii/S0888327019301153.

[14] J. Antoni, F. Bonnardot, A. Raad, M. El Badaoui, Cyclostationary modelling of rotating machine vibration signals, Mech. Syst. Signal Process. 18 (6) (2004) 1285–1314, http://dx.doi.org/10.1016/S0888-3270(03)00088-8, URL: https://linkinghub.elsevier.com/retrieve/pii/S0888327003000888.

[15] P.D. McFadden, J.D. Smith, Vibration monitoring of rolling element bearings by the high-frequency resonance technique — a review, Tribol. Int. 17 (1) (1984) 3–10, http://dx.doi.org/10.1016/0301-679X(84)90076-8, URL: https://www.sciencedirect.com/science/article/pii/0301679X84900768.

[16] R.B. Randall, J. Antoni, S. Chobsaard, The relationship between spectral correlation and envelope analysis in the diagnostics of bearing faults and other cyclostationary machine signals, Mech. Syst. Signal Process. 15 (5) (2001) 945–962, http://dx.doi.org/10.1006/mssp.2001.1415, URL: https://www.sciencedirect.com/science/article/pii/S0888327001914153.

[17] D. Abboud, J. Antoni, Order-frequency analysis of machine signals, Mech. Syst. Signal Process. 87 (2017) 229–258, http://dx.doi.org/10.1016/j.ymssp.2016.10.024, URL: https://linkinghub.elsevier.com/retrieve/pii/S0888327016304368.

[18] J.T.Y. Cheung, G. Stephanopoulos, Representation of process trends—Part I. A formal representation framework, Comput. Chem. Eng. 14 (4) (1990) 495–510, http://dx.doi.org/10.1016/0098-1354(90)87023-I, URL: https://www.sciencedirect.com/science/article/pii/009813549087023I.

[19] M.G. Kendall, A new measure of rank correlation, Biometrika 30 (1–2) (1938) 81–93, http://dx.doi.org/10.1093/biomet/30.1-2.81, URL: https://academic.oup.com/biomet/article-lookup/doi/10.1093/biomet/30.1-2.81.

[20] H.B. Mann, Nonparametric tests against trend, Econometrica 13 (3) (1945) 245–259, http://dx.doi.org/10.2307/1907187, URL: https://www.jstor.org/stable/1907187. Publisher: [Wiley, Econometric Society].

[21] M.G. Kendall, J.D. Gibbons, M.G. Kendall, Rank Correlation Methods, fifth ed., Oxford Univ. Press, New York, 1990.

[22] K.H. Hamed, A. Ramachandra Rao, A modified Mann-Kendall trend test for autocorrelated data, J. Hydrol. 204 (1) (1998) 182–196, http://dx.doi.org/10.1016/S0022-1694(97)00125-X, URL: https://www.sciencedirect.com/science/article/pii/S002216949700125X.

[23] T.B. Fomby, T.J. Vogelsang, The application of size-robust trend statistics to global-warming temperature series, J. Clim. 15 (1) (2002) 117–123, http://dx.doi.org/10.1175/1520-0442(2002)015<0117:TAOSRT>2.0.CO;2, URL: https://journals.ametsoc.org/view/journals/clim/15/1/1520-0442_2002_015_0117_taosrt_2.0.co_2.xml. Publisher: American Meteorological Society Section: Journal of Climate.

[24] A. Gadgil, A. Dhorde, Temperature trends in twentieth century at Pune, India, Atmos. Environ. 39 (35) (2005) 6550–6556, http://dx.doi.org/10.1016/j.atmosenv.2005.07.032, URL: https://www.sciencedirect.com/science/article/pii/S1352231005006540.

[25] M. Gocic, S. Trajkovic, Analysis of changes in meteorological variables using Mann-Kendall and Sen's slope estimator statistical tests in Serbia, Glob. Planet. Change 100 (2013) 172–182, http://dx.doi.org/10.1016/j.gloplacha.2012.10.014, URL: https://www.sciencedirect.com/science/article/pii/S0921818112002032.

[26] Y.S. Güçlü, Multiple Şen-innovative trend analyses and partial Mann-Kendall test, J. Hydrol. 566 (2018) 685–704, http://dx.doi.org/10.1016/j.jhydrol.2018.09.034, URL: https://www.sciencedirect.com/science/article/pii/S0022169418307285.

[27] P. Li, X. Jia, J. Feng, H. Davari, G. Qiao, Y. Hwang, J. Lee, Prognosability study of ball screw degradation using systematic methodology, Mech. Syst. Signal Process. 109 (2018) 45–57, http://dx.doi.org/10.1016/j.ymssp.2018.02.046, URL: https://www.sciencedirect.com/science/article/pii/S0888327018301109.

[28] M. Moradi, A. Broer, J. Chiachío, R. Benedictus, T.H. Loutas, D. Zarouchas, Intelligent health indicator construction for prognostics of composite structures utilizing a semi-supervised deep neural network and SHM data, Eng. Appl. Artif. Intell. 117 (2023) 105502, http://dx.doi.org/10.1016/j.engappai.2022.105502, URL: https://linkinghub.elsevier.com/retrieve/pii/S0952197622004924.

[29] Z. Xu, M. Bashir, Q. Liu, Z. Miao, X. Wang, J. Wang, N. Ekere, A novel health indicator for intelligent prediction of rolling bearing remaining useful life based on unsupervised learning model, Comput. Ind. Eng. 176 (2023) 108999, http://dx.doi.org/10.1016/j.cie.2023.108999, URL: https://www.sciencedirect.com/science/article/pii/S0360835223000232.

[30] V. Vakharia, V.K. Gupta, P.K. Kankar, A comparison of feature ranking techniques for fault diagnosis of ball bearing, Soft Comput. 20 (4) (2016) 1601–1619, http://dx.doi.org/10.1007/s00500-015-1608-6.

[31] L. Pinciroli, P. Baraldi, A. Shokry, E. Zio, R. Seraoui, C. Mai, A semi-supervised method for the characterization of degradation of nuclear power plants steam generators, Prog. Nucl. Energy 131 (2021) 103580, http://dx.doi.org/10.1016/j.pnucene.2020.103580, URL: https://www.sciencedirect.com/science/article/pii/S0149197020303279.

[32] K. Lyu, X. Tan, G. Liu, C. Zhao, Sensor selection of helicopter transmission systems based on physical model and sensitivity analysis, Chin. J. Aeronaut. 27 (3) (2014) 643–654, http://dx.doi.org/10.1016/j.cja.2014.04.025, URL: https://linkinghub.elsevier.com/retrieve/pii/S1000936114000958.

[33] F. Guo, B. Rasmussen, Predictive maintenance for residential air conditioning systems with smart thermostat data using modified Mann-Kendall tests, Appl. Therm. Eng. 222 (2023) 119955, http://dx.doi.org/10.1016/j.applthermaleng.2022.119955, URL: https://www.sciencedirect.com/science/article/pii/S1359431122018853.

[34] S. Yue, P. Pilon, A comparison of the power of the *t* test, Mann-Kendall and bootstrap tests for trend detection / Une comparaison de la puissance des tests *t* de Student, de Mann-Kendall et du bootstrap pour la détection de tendance, Hydrol. Sci. J. 49 (1) (2004) 21–37, http://dx.doi.org/10.1623/hysj.49.1.21.53996, URL: https://www.tandfonline.com/doi/full/10.1623/hysj.49.1.21.53996.

[35] M.G. Kendall, The treatment of ties in ranking problems, Biometrika 33 (3) (1945) 239–251, http://dx.doi.org/10.2307/2332303, URL: https://www.jstor.org/stable/2332303. Publisher: [Oxford University Press, Biometrika Trust].

[36] R.M. Hirsch, J.R. Slack, R.A. Smith, Techniques of trend analysis for monthly water quality data, Water Resour. Res. 18 (1) (1982) 107–121, http://dx.doi.org/10.1029/WR018i001p00107, URL: https://onlinelibrary.wiley.com/doi/abs/10.1029/WR018i001p00107. _eprint: https://onlinelibrary.wiley.com/doi/pdf/10.1029/WR018i001p00107.

[37] R.M. Hirsch, J.R. Slack, A nonparametric trend test for seasonal data with serial dependence, Water Resour. Res. 20 (6) (1984) 727–732, http://dx.doi.org/10.1029/WR020i006p00727, URL: https://onlinelibrary.wiley.com/doi/abs/10.1029/WR020i006p00727. _eprint: https://onlinelibrary.wiley.com/doi/pdf/10.1029/WR020i006p00727.

[38] S. Yue, C.Y. Wang, Applicability of prewhitening to eliminate the influence of serial correlation on the Mann-Kendall test, Water Resour. Res. 38 (6) (2002) 4–1–4–7, http://dx.doi.org/10.1029/2001WR000861, URL: https://onlinelibrary.wiley.com/doi/abs/10.1029/2001WR000861. _eprint: https://onlinelibrary.wiley.com/doi/pdf/10.1029/2001WR000861.

[39] W.A. Shewhart, Control of Quality of Manufactured Product, Bell Telephone Laboratories, 1929.

[40] M. Basseville, I.V. Nikiforov, Detection of Abrupt Changes: Theory and Application, in: Prentice Hall Information and System Sciences Series, Prentice Hall, Englewood Cliffs, N.J, 1993.

[41] K.H. Hamed, Exact distribution of the Mann–Kendall trend test statistic for persistent data, J. Hydrol. 365 (1) (2009) 86–94, http://dx.doi.org/10.1016/j.jhydrol.2008.11.024, URL: https://www.sciencedirect.com/science/article/pii/S0022169408005787.

[42] F. Bonnardot, M. El Badaoui, R.B. Randall, J. Danière, F. Guillet, Use of the acceleration signal of a gearbox in order to perform angular resampling (with limited speed fluctuation), Mech. Syst. Signal Process. 19 (4) (2005) 766–785, http://dx.doi.org/10.1016/j.ymssp.2004.05.001, URL: https://www.sciencedirect.com/science/article/pii/S0888327004000664.

[43] E.J. Cross, K. Worden, Q. Chen, Cointegration: a novel approach for the removal of environmental trends in structural health monitoring data, Proc. R. Soc. A: Math. Phys. Eng. Sci. 467 (2133) (2011) 2712–2732, http://dx.doi.org/10.1098/rspa.2011.0023, URL: https://royalsocietypublishing.org/doi/10.1098/rspa.2011.0023. Publisher: Royal Society.

[44] E.J. Cross, K. Worden, Cointegration and why it works for SHM, J. Phys. Conf. Ser. 382 (1) (2012) 012046, http://dx.doi.org/10.1088/1742-6596/382/1/012046.

[45] H. André, F. Allemand, I. Khelf, A. Bourdon, D. Rémond, Improving the monitoring indicators of a variable speed wind turbine using support vector regression, Appl. Acoust. 166 (2020) 107350, http://dx.doi.org/10.1016/j.apacoust.2020.107350, URL: https://www.sciencedirect.com/science/article/pii/S0003682X18312015.

[46] J. McBain, M. Timusk, Fault detection in variable speed machinery: Statistical parameterization, J. Sound Vib. 327 (3) (2009) 623–646, http://dx.doi.org/10.1016/j.jsv.2009.07.025, URL: https://www.sciencedirect.com/science/article/pii/S0022460X09005896.

[47] J. Antoni, Cyclic spectral analysis of rolling-element bearing signals: Facts and fictions, J. Sound Vib. 304 (3–5) (2007) 497–529, http://dx.doi.org/10.1016/j.jsv.2007.02.029, URL: https://linkinghub.elsevier.com/retrieve/pii/S0022460X07001551.

[48] J. Antoni, R. Randall, The spectral kurtosis: application to the vibratory surveillance and diagnostics of rotating machines, Mech. Syst. Signal Process. 20 (2) (2006) 308–331, http://dx.doi.org/10.1016/j.ymssp.2004.09.002, URL: https://linkinghub.elsevier.com/retrieve/pii/S0888327004001529.

[49] J. Antoni, Fast computation of the kurtogram for the detection of transient faults, Mech. Syst. Signal Process. 21 (1) (2007) 108–124, http://dx.doi.org/10.1016/j.ymssp.2005.12.002, URL: https://www.sciencedirect.com/science/article/pii/S0888327005002414.

[50] T. Barszcz, A. Jabłoński, A novel method for the optimal band selection for vibration signal demodulation and comparison with the Kurtogram, Mech. Syst. Signal Process. 25 (1) (2011) 431–451, http://dx.doi.org/10.1016/j.ymssp.2010.05.018, URL: https://www.sciencedirect.com/science/article/pii/S0888327010001895.
[51] Y. Lei, J. Lin, Z. He, Y. Zi, Application of an improved kurtogram method for fault diagnosis of rolling element bearings, Mech. Syst. Signal Process. 25 (5) (2011) 1738–1749, http://dx.doi.org/10.1016/j.ymssp.2010.12.011, URL: https://www.sciencedirect.com/science/article/pii/S0888327011000033.
[52] P.W. Tse, D. Wang, The design of a new sparsogram for fast bearing fault diagnosis: Part 1 of the two related manuscripts that have a joint title as "Two automatic vibration-based fault diagnostic methods using the novel sparsity measurement – Parts 1 and 2", Mech. Syst. Signal Process. 40 (2) (2013) 499–519, http://dx.doi.org/10.1016/j.ymssp.2013.05.024, URL: https://www.sciencedirect.com/science/article/pii/S0888327013002914.
[53] B. Hou, D. Wang, T. Xia, L. Xi, Z. Peng, K.-L. Tsui, Generalized Gini indices: Complementary sparsity measures to Box-Cox sparsity measures for machine condition monitoring, Mech. Syst. Signal Process. 169 (2022) 108751, http://dx.doi.org/10.1016/j.ymssp.2021.108751, URL: https://www.sciencedirect.com/science/article/pii/S0888327021010670.
[54] J. Antoni, The infogram: Entropic evidence of the signature of repetitive transients, Mech. Syst. Signal Process. 74 (2016) 73–94, http://dx.doi.org/10.1016/j.ymssp.2015.04.034, URL: https://www.sciencedirect.com/science/article/pii/S0888327015002174.
[55] A. Moshrefzadeh, A. Fasana, The Autogram: An effective approach for selecting the optimal demodulation band in rolling element bearings diagnosis, Mech. Syst. Signal Process. 105 (2018) 294–318, http://dx.doi.org/10.1016/j.ymssp.2017.12.009, URL: https://www.sciencedirect.com/science/article/pii/S0888327017306441.
[56] A. Mauricio, K. Gryllias, Cyclostationary-based multiband envelope spectra extraction for bearing diagnostics: The combined improved envelope spectrum, Mech. Syst. Signal Process. 149 (2021) 107150, http://dx.doi.org/10.1016/j.ymssp.2020.107150, URL: https://www.sciencedirect.com/science/article/pii/S0888327020305367.
[57] M.R. Hoeprich, Rolling element bearing fatigue damage propagation, J. Tribol. 114 (2) (1992) 328–333, http://dx.doi.org/10.1115/1.2920891, URL: https://asmedigitalcollection.asme.org/tribology/article/114/2/328/434142/Rolling-Element-Bearing-Fatigue-Damage-Propagation.
[58] A.V. Olver, The mechanism of rolling contact fatigue: An update, Proc. Inst. Mech. Eng. J 219 (5) (2005) 313–330, http://dx.doi.org/10.1243/135065005X9808, URL: http://journals.sagepub.com/doi/10.1243/135065005X9808.
[59] P. Rycerz, A. Olver, A. Kadiric, Propagation of surface initiated rolling contact fatigue cracks in bearing steel, Int. J. Fatigue 97 (2017) 29–38, http://dx.doi.org/10.1016/j.ijfatigue.2016.12.004, URL: https://www.sciencedirect.com/science/article/pii/S014211231630411X.
[60] R.B. Randall, Efficient Machine Monitoring Using a Calculator-Based System, Manchester, UK, 1979.
[61] R. Randall, Computer-aided vibration spectrum trend analysis for condition monitoring, Maint. Manag. Int. 5 (3) (1985) 161–167, Publisher: ELSEVIER SCIENCE BV PO BOX 211, 1000 AE AMSTERDAM, NETHERLANDS.
[62] P. Bradshaw, R. Randall, Early detection and diagnosis of machine faults on the Trans Alaska pipeline, in: MSA Session, ASME Conference, Dearborn, Mich, 1983.
[63] L.D. Meyer, F.F. Ahlgren, B. Weichbrodt, An analytic model for ball bearing vibrations to predict vibration response to distributed defects, J. Mech. Des. 102 (2) (1980) 205–210, http://dx.doi.org/10.1115/1.3254731, URL: https://asmedigitalcollection.asme.org/mechanicaldesign/article/102/2/205/430940/An-Analytic-Model-for-Ball-Bearing-Vibrations-to.
[64] A. Marsick, H. André, I. Khelf, Q. Leclère, J. Antoni, Restoring cyclostationarity of rolling element bearing signals from the instantaneous phase of their envelope, Mech. Syst. Signal Process. 193 (2023) 110264, http://dx.doi.org/10.1016/j.ymssp.2023.110264, URL: https://www.sciencedirect.com/science/article/pii/S0888327023001711.
[65] R. Bertoni, H. André, Proposition of a bearing diagnosis method applied to IAS and vibration signals: The BEAring Frequency Estimation Method, Mech. Syst. Signal Process. 187 (2023) 109891, http://dx.doi.org/10.1016/j.ymssp.2022.109891, URL: https://www.sciencedirect.com/science/article/pii/S0888327022009591.
[66] F. Crameri, Scientific colour maps, 2018, http://dx.doi.org/10.5281/zenodo.5501399, URL: https://zenodo.org/record/5501399. Language: eng.
[67] F. Crameri, G.E. Shephard, P.J. Heron, The misuse of colour in science communication, Nature Commun. 11 (1) (2020) 5444, http://dx.doi.org/10.1038/s41467-020-19160-7, URL: https://www.nature.com/articles/s41467-020-19160-7. Number: 1 Publisher: Nature Publishing Group.